NICKEL(II) TETRAPHENYLPORPHYRIN: CORE-SHELL NANOPARTICLE SYNTHESIS, CHARACTERIZATION, AND MAGNETIC PROPERTIES

A Thesis

Presented to

The Faculty of the Department of Physics and Astronomy

California State University, Los Angeles

In Partial Fulfillment

of the Requirements for the Degree

Bachelor of Science

in

Physics

By

Cristian Reynaga Gonzalez

May 2024

© 2024

Cristian Reynaga Gonzalez

ALL RIGHTS RESERVED

The thesis of Cristian Reynaga Gonzalez is approved.

Professor Armen Kocharian, Committee Member

Professor Oscar Bernal, Committee Member

Professor Radi Jishi, Department Chair

California State University, Los Angeles

May 2024

ABSTRACT

Nickel(II) Tetraphenylporphyrin: Core-Shell Nanoparticle Synthesis,

Characterization, and Magnetic Properties

By

Cristian Reynaga Gonzalez

The exploration of Nickel(II) Tetraphenylporphyrin (NiTPP) under thermal decomposition provides crucial insights into synthesizing novel magnetic materials with potential applications in nanotechnology and biomedical applications. This study investigates the structural evolution and magnetic behavior of NiTPP subjected to solid-phase pyrolysis at varying temperatures (500°C - 900°C) and times (10 - 240 minutes). Through a range of characterization techniques, including Powder X-ray Diffraction (PXRD), Physical Property Measurement System (PPMS) with Vibrating Sample Magnetometry (VSM), and Scanning Electron Microscopy (SEM), we attempt to interpret the interplay between pyrolysis conditions and the resultant nanoparticle properties. The emergence of magnetic core-shell structures and the impact of subsequent annealing in oxygen and nitrogen atmospheres on the nanoparticles' morphology and magnetic properties are investigated. As we compare our initial NiTPP findings with previous work, we aim to replicate and refine synthesis procedures for various metal centers within the porphyrin matrix, including cobalt, copper, and zinc. In doing so, we attempt to identify pathways that allow the tailoring of morphology and magnetic characteristics in nanoparticles.

ACKNOWLEDGMENTS

I would like to extend my deepest gratitude to the Minority Opportunities in Research (MORE) Programs, particularly the MARC USTAR Programs, and Dr. Linda Tunstad, Co-Director of MORE Programs and Program Director of Bridges to the Future and MARC USTAR Programs, for their invaluable support. I am also thankful to the Center for Energy and Sustainability and the Centers for Research Excellence in Science and Technology (CREST) program; their funding was instrumental in the success of this research.

A heartfelt thank you to Professor Kocharian and Professor Bernal for their exceptional mentorship. I am immensely grateful to Armond Khodagulyan for his unwavering help and patience in the laboratory; he is the cornerstone of our lab's success. I would also like to acknowledge my lab mates, Jonah, Vicente, Sarah, Erick, and Franco, for their support and friendship.

Lastly, I am deeply appreciative of my loving wife Debra, my wonderful children Tristan and Nathan, and my family. This work is dedicated to you.

TABLE OF CONTENTS

Abstract iv

Acknowledgments v

List of Tables viii

List of Figures ix

Chapter

1. Introduction 1

1.1. The Evolution of Nanoparticles in Modern Science 1

1.2. Nanoparticles 3

1.3. Magnetic Nanoparticles 6

1.3.1. Basic Concepts of Magnetism 6

1.3.2. Nickel-Based Magnetic Nanoparticles 8

1.4. Core-Shell Nanoparticles 11

1.5. Nickel (II) Tetraphenylporphyrin (NiTPP) 12

1.6. Magnetic Hyperthermia and Biomedical Applications 14

2. Sample Synthesis and Experimental Technique 17

2.1. Sample and Ampoule Preparation 17

2.2. Solid-Phase Pyrolysis 19

2.3. Annealing 21

2.4. Deagglomeration Process 24

2.5. Powder X-ray Diffractometry 26

2.6. Scanning Electron Microscopy 27

2.7. Vibrating Sample Magnetometry 29

3. Results and Discussion 32

3.1. SEM Results 34

3.2. PXRD Results 39

3.3. VSM Results 45

3.4. Discussion 50

References 54

LIST OF TABLES

Table

1.1. Summary of nanoparticle synthesis techniques, their descriptions, and approach. 5

3.1. Summary of NiTPP core-shell nanoparticle samples, their synthesis conditions, and treatments. All annealing was performed at 150°C for 180 min, with a gas flow rate of 100 sccm. 33

3.2. Summary of the calculated grain sizes of nickel NPs synthesized at 900°C for various durations and annealed in O_2 and N_2 environments. Grain sizes were determined using Profex software through the application of the Scherrer equation to the PXRD data. 45

LIST OF FIGURES

Figure

1.1. The image shows the size range of various entities, from small molecules like Remdesivir to large objects like an apple, highlighting nanoparticles such as lipid NPs, gold nanoclusters, polymeric NPs, fullerenes, and ZIF-8 within the 1-100 nm scale. 3

1.2. A typical hysteresis loop for MNPs, highlighting the key features: saturation magnetization (M_s), remanent magnetization (M_r), and coercivity (H_c). 7

1.3. Illustration of atomic magnetic moment orientations in various magnetic states: (a) Diamagnetic, (b) Paramagnetic, (c) Ferromagnetic, (d) Ferrimagnetic, and (e) antiferromagnetic with and without an external magnetic field. 8

1.4. Illustrating the FCC crystal structure: (left) close-packed arrangement of atoms, (middle) schematic of the FCC unit cell with atoms at the corners and centers of each face, and (right) three-dimensional view of the FCC lattice. 10

1.5. Different core-shell and encapsulated structures including core-shell, yolk-shell, sandwiched core-shell, multi-core-shell, multi-core hollow structure, embedded structure, and core within mesoporous shells. . . 11

1.6. Molecular structure of Nickel(II) Tetraphenylporphyrin (NiTPP), a coordination compound where a nickel ion is centrally coordinated to a tetraphenylporphyrin ligand. 13

1.7. Schematic representation of magnetic hyperthermia treatment. MNPs are injected into the tumor site (left images). When subjected to an alternating magnetic field (right images), the MNPs generate localized heat, leading to the selective necrosis of cancer cells in tumors. 15

2.1. Sealing of a quartz ampoule using an oxy-acetylene torch. The ampoule contains precursor materials for the synthesis of carbon-coated core-shell nanoparticles. 18

2.2. MTI OTF-1200X-II-UL two-zone tube furnace used for solid-phase pyrolysis. An attached gas tank supplies the necessary atmosphere to ensure controlled reaction conditions during annealing. 20

2.3. The diagram illustrates the temperature profiles for different durations of the pyrolysis process, including heating and cooling rates of 9.7°C/min. The color-coded lines represent different hold times at 900°C: 60 minutes (black), 120 minutes (red), 180 minutes (blue), and 240 minutes (green). 20

2.4. Annealing ramp used in the experiment. 23

2.5. Figure illustrates the steps and instruments implemented during the deagglomeration process. 24

2.6. Schematic representation of Energy-Dispersive X-ray Spectroscopy (EDS). External stimulation causes an electron to be ejected from an atom's inner shell (K shell). As electrons from higher energy levels (L and M shells) fill the vacancy, characteristic X-rays, Kα, Kβ, and Lα are emitted, allowing for the identification of the sample's elemental composition. 28

2.7. PPMS sample holder secured in a brass sample holder and positioned in an alignment station. 30

3.1. NiTPP900C60mC SEM image and EDS elemental mapping of the synthesized NiTPP nanoparticles, showing the distribution of nickel, carbon, nitrogen, and oxygen elements. 34

3.2. NiTPP900C60mOC SEM image and EDS elemental mapping of the synthesized NiTPP nanoparticles, showing the distribution of nickel, carbon, nitrogen, and oxygen elements. 35

3.3. NiTPP900C60mNC SEM image and EDS elemental mapping of the synthesized NiTPP nanoparticles, showing the distribution of nickel, carbon, nitrogen, and oxygen elements. 36

3.4. NiTPP900C240mC SEM image and EDS elemental mapping of the synthesized NiTPP nanoparticles, showing the distribution of nickel, carbon, nitrogen, and oxygen elements. 37

3.5. NiTPP900C240mOC SEM image and EDS elemental mapping of the synthesized NiTPP nanoparticles, showing the distribution of nickel, carbon, nitrogen, and oxygen elements. 38

3.6. NiTPP900C240mNC SEM image and EDS elemental mapping of the synthesized NiTPP nanoparticles, showing the distribution of nickel, carbon, nitrogen, and oxygen elements. 38

3.7. PXRD pattern of the Nickel(II) Tetraphenylporphyrin (NiTPP) precursor before pyrolysis. The peaks correspond to the crystalline structure of the organic compound. 40

3.8. PXRD patterns of NiTPP synthesized at 900°C for 60 minutes: (a) No Annealing, (b) Annealed in O at 150°C for 180 minutes, and (c) Annealed in N at 150°C for 180 minutes.The diffraction peaks correspond to FCC Ni (111), (200), (220), (311), (222), and graphite (2H and 3R) structures. 41

3.9. PXRD patterns of NiTPP synthesized at 900°C for 120 minutes: (a) No Annealing, (b) Annealed in O at 150°C for 180 minutes, and (c) Annealed in N at 150°C for 180 minutes.The diffraction peaks correspond to FCC Ni (111), (200), (220), (311), (222), and graphite (2H and 3R) structures 42

3.10. PXRD patterns of NiTPP synthesized at 900°C for 180 minutes: (a) No Annealing, (b) Annealed in O at 150°C for 180 minutes, and (c) Annealed in N at 150°C for 180 minutes.The diffraction peaks correspond to FCC Ni (111), (200), (220), (311), (222), and graphite (2H and 3R) structures 43

3.11. PXRD patterns of NiTPP synthesized at 900°C for 240 minutes: (a) No Annealing, (b) Annealed in O at 150°C for 180 minutes, and (c) Annealed in N at 150°C for 180 minutes.The diffraction peaks correspond to FCC Ni (111), (200), (220), (311), (222), and graphite (2H and 3R) structures 43
3.12. Hysteresis loops of NiTPP precursor measured at 10K and 300K. . . 46
3.13. Hysteresis loops of NiTPP samples synthesized at 900°C for 60 minutes, measured at 300K. 47
3.14. Hysteresis loops of NiTPP samples synthesized at 900°C for 60 minutes, measured at 10K. 48
3.15. Hysteresis loops of NiTPP samples synthesized at 900°C for 120 minutes, measured at 300K. 49
3.16. Hysteresis loops of NiTPP samples synthesized at 900°C for 180 minutes, measured at 300K. 50
3.17. Hysteresis loops of NiTPP samples synthesized at 900°C for 240 minutes, measured at 300K. 51

CHAPTER 1

Introduction

1.1 The Evolution of Nanoparticles in Modern Science

Fundamental discoveries and innovations have driven the evolution of nanotechnology, advancing our ability to understand and manipulate materials at the nanoscale. One of the earliest known applications of nanoparticles (NPs) dates to ancient Rome, exemplified by the Lycurgus Cup from the 4th century AD. This dichroic cup, which changes color based on the direction of light, demonstrates the use of gold and silver NPs, showcasing early, albeit unintentional, nanoparticle manipulation. In the 19th century, Michael Faraday made groundbreaking contributions to the field with his work on colloidal gold. In 1857, Faraday observed the distinct color changes of gold colloids due to variations in particle size, hypothesized the existence of metallic particles at the nanoscale, and developed techniques to synthesize and stabilize these colloids[1]. His observations laid the groundwork for colloidal chemistry and NPs research.

The idea of nanotechnology was further advanced in the 20th century by Richard Feynman. In his seminal 1959 lecture, "There's Plenty of Room at the Bottom," Feynman articulated a vision for manipulating matter at the atomic and molecular levels, predicting the vast potential of nanoscale engineering [2]. This foresight spurred the scientific community to explore the possibilities of working at such

diminutive scales. Thirty years later, a technological breakthrough came in 1981 with the invention of the scanning tunneling microscope (STM) by Gerd Binnig and Heinrich Rohrer. This device enabled direct visualization and manipulation of individual atoms on surfaces, a capability that earned its inventors the Nobel Prize in Physics in 1986 [3]. The STM's ability to produce atomic-resolution images revolutionized surface science and catalyzed advancements in nanotechnology.

The discovery of carbon-based nanomaterials in the 1980s and 1990s was pivotal. Fullerenes (buckyballs) were discovered by Harold Kroto, Richard Smalley, and Robert Curl in 1985[4], and carbon nanotubes were discovered by Sumio Iijima in 1991[5]. These materials exhibited unique structural, electrical, and mechanical properties, expanding nanomaterials' applications in electronics, materials science, and medicine. The significance of fullerenes was highlighted by the Nobel Prize in Chemistry awarded to their discoverers in 1996. The early 21st century saw further advancements in NPs synthesis techniques. Methods such as chemical vapor deposition (CVD), sol-gel processes, and hydrothermal synthesis enabled precise control over NPs size, shape, and composition [6]. These techniques have facilitated the integration of NPs into applications ranging from targeted drug delivery systems and diagnostic tools to energy storage devices and environmental remediation [7]. Currently, nanotechnology research is characterized by developing multi-functional NPs capable of performing simultaneous tasks, such as targeted drug delivery and real-time imaging [8]. In the biomedical field, researchers are developing NPs for targeted drug delivery, diagnostic imaging, and therapeutic agents in cancer treatment. Magnetic nanoparticles (MNPs), in particular, have garnered attention for their use in mag-

netic resonance imaging (MRI) and magnetic hyperthermia therapy [9]. The interdisciplinary nature of modern nanoparticle research has allowed fields like biomedicine, electronics, and environmental science to benefit from advancements in targeted drug delivery, enhanced imaging techniques, and environmental remediation technologies.

1.2 Nanoparticles

Nanoparticles, defined as particles with diameters between 1 nm and 100 nm, see Figure 1.1, exhibit unique properties significantly different from their bulk counterparts due to their high surface-to-volume ratio and quantum effects [10].

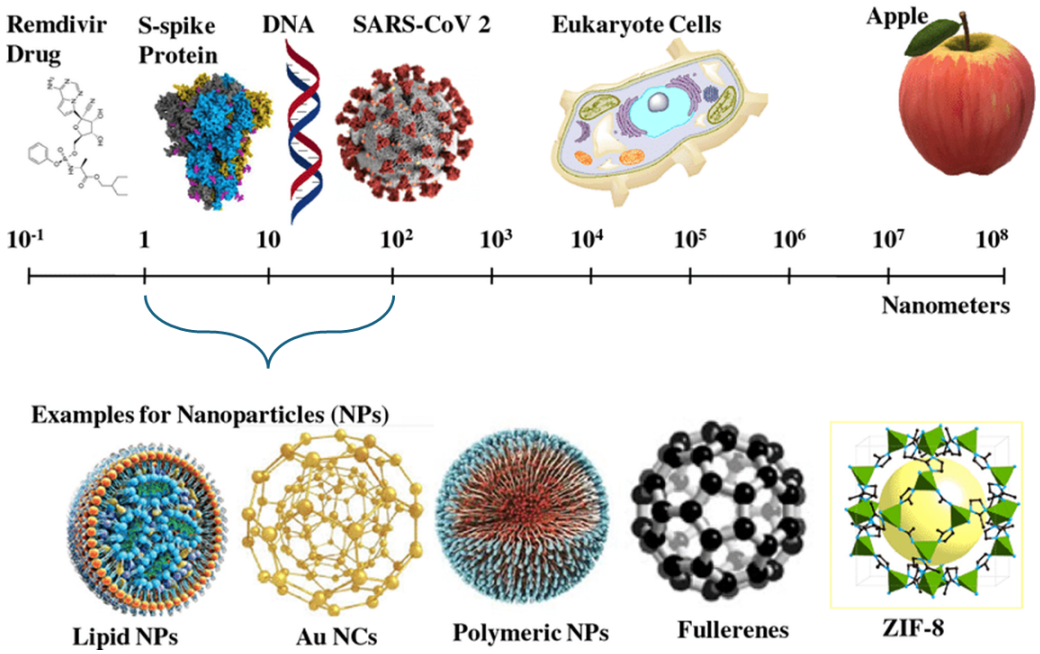


Figure 1.1: The image shows the size range of various entities, from small molecules like Remdesivir to large objects like an apple, highlighting nanoparticles such as lipid NPs, gold nanoclusters, polymeric NPs, fullerenes, and ZIF-8 within the 1-100 nm scale.

These particles can be synthesized from various inorganic and organic materials through two general methodological approaches: bottom-up and top-down techniques. In the bottom-up approach, NPs are assembled from smaller units, such as

atoms or molecules, through chemical processes. In contrast, the top-down approach involves breaking down bulk materials into smaller particles. Numerous synthesis techniques fall under the bottom-up category, offering specific advantages in controlling the NPs' size, shape, and composition. Some of the widely used synthesis methods are listed in Table 1.1. Because of their small dimensions, NPs are not readily observable with optical microscopes. This limitation arises because the wavelength of visible light ranges from 380 to 700 nanometers and is significantly larger than the size of even the largest NPs. As a result, optical light microscopes, which rely on visible light for imaging, cannot resolve objects as small as NPs, rendering these microscopes ineffective. The inability of optical microscopes to visualize NPs stems from the fundamental diffraction limit, which restricts the resolution of these microscopes to about half the wavelength of the light used. Thus, advanced techniques are required. Electron microscopy, for instance, uses electron beams with much shorter wavelengths than visible light, allowing for high-resolution imaging at the nanoscale. Other methods, such as scanning tunneling microscopy (STM) and atomic force microscopy (AFM), also enable detailed visualization and characterization of NPs by probing the surface at the atomic level.

Technique	**Description**	**Approach**
Co-precipitation	A method involving the simultaneous precipitation of components from a solution. [11]	Bottom-Up
Thermal Decomposition	Involves high-temperature decomposition of precursors under vacuum, air, or gases. [12]	Bottom-Up
Hydrothermal and Solvothermal Synthesis	High-temperature and pressure reactions in aqueous or non-aqueous solvents. [13]	Bottom-Up
Sol-Gel Process	The sol-gel process transitions a system from a liquid 'sol' to a solid 'gel' phase by hydrolysis and condensation reactions. [14]	Bottom-Up
Flame Spray Pyrolysis	Uses high-temperature flames to produce nanoparticles from liquid precursors. [15]	Bottom-Up
Sonochemical Synthesis	Ultrasonic waves induce chemical reactions, forming nanostructured materials. [16]	Bottom-Up
Vapor Deposition	Vaporized materials condense to form nanoparticles on a substrate, including chemical and physical vapor deposition methods. [17]	Bottom-Up
Microwave-Assisted Synthesis	Rapid and uniform heating by microwaves accelerates chemical reactions. [18]	Bottom-Up
Polyol Process	A high-boiling point polyol acts as a solvent and reducing agent. [19]	Bottom-Up
Mechanical Milling	Involves the mechanical grinding of bulk materials into fine particles using ball mills. [20]	Top-Down
Pulsed Laser Ablation	High-power laser pulses are used to vaporize materials, producing nanoparticles from the condensed vapor. [21]	Top-Down

Table 1.1: Summary of nanoparticle synthesis techniques, their descriptions, and approach.

1.3 Magnetic Nanoparticles

1.3.1 Basic Concepts of Magnetism

To comprehend the magnetic properties of NPs, it is essential to understand the fundamental concepts of magnetism. Magnetism is a physical phenomenon mediated by magnetic fields. Electric currents and the magnetic moments of elementary particles give rise to these fields. Specifically, electrons' orbital and spin motions and their interactions generate magnetic fields. The combination of spin-orbit coupling and various electron interaction types results in a wide range of magnetic phenomena.

Magnetization (M) is defined as the magnetic moment per unit volume of a material and varies with the applied magnetic field strength (H), but can also be expressed per unit mass (emu/g). When a magnetic material is subjected to a magnetic field, the resultant magnetic induction (B) is given by:

$$B = H + 4\pi M \tag{1.1}$$

In CGS units, the permeability of free space is equal to one and thus does not appear in the equation. The volumetric magnetic susceptibility (χ) quantifies the degree to which a material can be magnetized in response to an applied magnetic field and is defined as:

$$M = \chi H \tag{1.2}$$

In CGS units, χ is dimensionless, and both M and H are expressed in oersteds (Oe).

The typical magnetization curve, as a function of the applied magnetic field, reveals key features such as saturation magnetization (M_s), remanent magnetization (M_r), and coercive field (H_c), see Figure 1.2. Saturation magnetization occurs when all magnetic dipoles align with the external magnetic field. Remanent magnetization is the residual magnetization when the external field is removed, and the coercive field is the reverse field required to reduce the magnetization to zero. Magnetic susceptibility in materials depends on temperature and the applied magnetic field[22], leading to the characteristic sigmoidal shape of the M vs H curve, with M approaching saturation at high magnetic field values. Hysteresis is a lag in the magnetization process often seen in ferromagnetic and ferrimagnetic materials. This happens because the magnetic regions in the material get stuck at impurities or boundaries and because the material's magnetic properties vary in different directions.

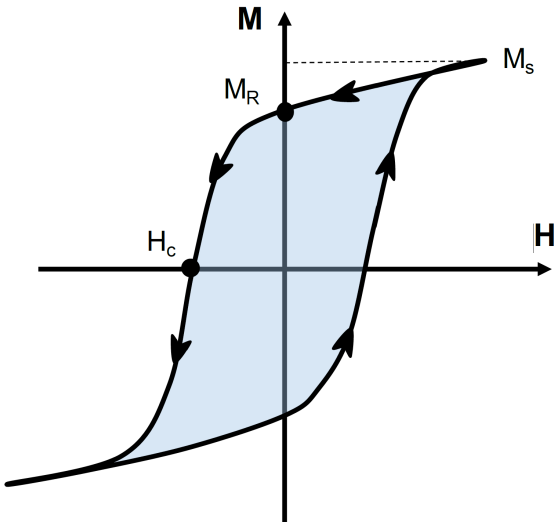


Figure 1.2: A typical hysteresis loop for MNPs, highlighting the key features: saturation magnetization (M_s), remanent magnetization (M_r), and coercivity (H_c).

1.3.2 Nickel-Based Magnetic Nanoparticles

All matter exhibits some form of magnetism. The key difference between materials lies in the extent of the collective interaction of atomic magnetic moments. Some materials show no significant collective interaction, while others display very strong interactions. We can classify magnetic properties by applying a magnetic field to these materials and observing their response. Generally, the magnetic behavior of materials is categorized as diamagnetism, paramagnetism, ferromagnetism, ferrimagnetism, and antiferromagnetism[23], as shown in Figure 1.3.

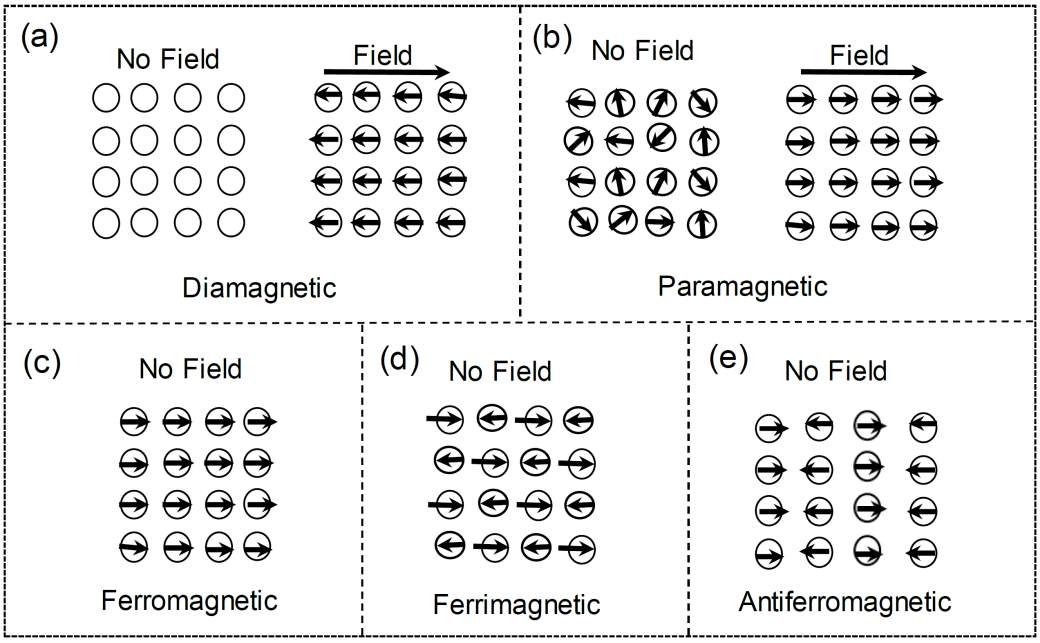


Figure 1.3: Illustration of atomic magnetic moment orientations in various magnetic states: (a) Diamagnetic, (b) Paramagnetic, (c) Ferromagnetic, (d) Ferrimagnetic, and (e) antiferromagnetic with and without an external magnetic field.

In addition to these categories, superparamagnetic behavior is commonly observed in nano and single-domain particles[24]. For this thesis, our discussion will focus solely on ferromagnetic behavior.

Ferromagnetism in materials such as iron (Fe), nickel (Ni), and cobalt (Co) originates from the interactions of unpaired electrons in their d-orbitals. These transition metals have partially filled 3d orbitals, contributing to their magnetic properties. The intense exchange interactions among these unpaired electrons lead to parallel alignment of their spins, resulting in a significant net magnetic moment without an external magnetic field.

The Curie temperature (T_C) is an important point for ferromagnetic materials. It is the temperature above which a ferromagnetic material loses its permanent magnetism and becomes paramagnetic. Below this temperature, the material remains ferromagnetic because the thermal energy is not strong enough to disrupt the magnetic order. Above the Curie temperature, the heat causes the magnetic moments to become misaligned, turning the material paramagnetic.

As previously mentioned, nickel, with an atomic number of 28, exhibits strong ferromagnetic properties that arise from its electronic structure. Nickel has an electron configuration of [Ar]$3d^8 4s^2$, with the partially filled 3d orbital that plays a crucial role in its magnetic properties, and its (T_C) is approximately 358°C (631 K). Nickel's high saturation magnetization makes it an excellent material for various magnetic applications. Nickel also exhibits significant magnetic anisotropy, affecting nickel-based magnetic materials' coercivity and remanence[25].

Nickel crystallizes in a face-centered cubic (FCC) structure, one of the most densely packed crystal structures. In the FCC structure, each nickel atom is surrounded by 12 nearest neighbors, forming a highly coordinated lattice, as illustrated in Figure 1.4. This arrangement contributes to nickel's stability, mechanical strength,

and magnetic properties.

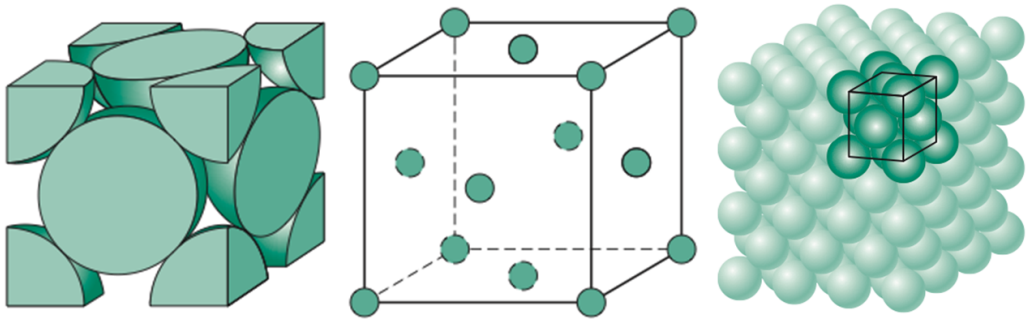


Figure 1.4: Illustrating the FCC crystal structure: (left) close-packed arrangement of atoms, (middle) schematic of the FCC unit cell with atoms at the corners and centers of each face, and (right) three-dimensional view of the FCC lattice.

The FCC structure of nickel plays a significant role in its ferromagnetic behavior[26]. The high coordination number and close packing of atoms facilitate strong exchange interactions between the unpaired 3d electrons, enhancing the ferromagnetic ordering. Additionally, the FCC structure allows for the formation of various nanoscale structures, such as NPs, nanowires, and thin films, which can be tailored for specific applications.

The ability to manipulate nickel's crystal structure and morphology at the nanoscale is crucial for developing advanced magnetic materials. By controlling the synthesis conditions, researchers can tailor nickel nanostructures' size, shape, and crystallinity to achieve the desired magnetic properties. For instance, nickel NPs with a well-defined FCC structure can exhibit enhanced saturation magnetization and reduced coercivity, making them excellent candidates for applications in magnetic hyperthermia, targeted drug delivery, and MRI contrast agents. These properties make nickel valuable for developing advanced MNPs with potential applications in

biomedicine and other fields.

1.4 Core-Shell Nanoparticles

Core-shell NPs are a class of nanostructures characterized by a core material encapsulated by a shell made of a different material. This architecture combines distinct properties from core and shell materials, resulting in multifunctional NPs with enhanced application performance. The core-shell structure is particularly advantageous in tuning NPs' chemical, physical, and biological properties, making them suitable for various applications, including catalysis, drug delivery, imaging, and magnetic applications. Many variations of core-shell NPs are presented in Figure 1.5.

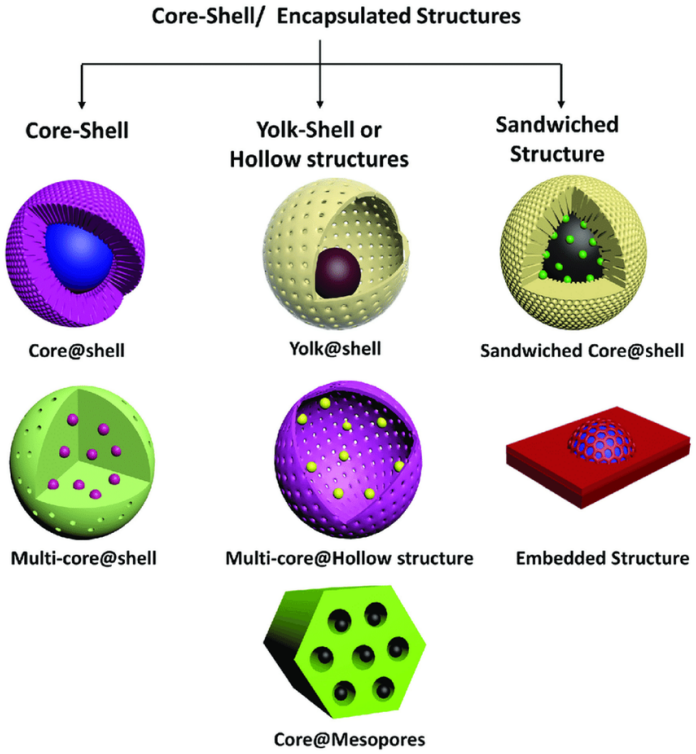


Figure 1.5: Different core-shell and encapsulated structures including core-shell, yolk-shell, sandwiched core-shell, multi-core-shell, multi-core hollow structure, embedded structure, and core within mesoporous shells.

The design of core-shell NPs involves selecting appropriate core and shell ma-

terials to achieve the desired properties. The core typically determines the primary functionality, while the shell provides stability, biocompatibility, or additional functionalities. The synthesis of core-shell NPs can be achieved through methods similar to those described in Table 1.1. These NPs offer several functional advantages due to their architecture, like enhanced stability, tailored surface properties, controlled release, and magnetic properties.

Core-shell MNPs have gained significant attention due to their potential applications in biomedical fields. The core typically comprises magnetic materials like iron oxide (Fe_3O_4), Co, or Ni. At the same time, the shell can be made of materials like carbon, silica, or polymers to provide biocompatibility and functionalization sites. For example, an iron oxide core encapsulated by a silica shell offers biocompatibility and can attach functional groups for targeted drug delivery[29]. The magnetic core enables imaging and hyperthermia treatment, while the silica shell ensures stability and controlled drug release.

Our research uses nickel (II) tetraphenylporphyrin (NiTPP) as a precursor for our core-shell synthesis. This precursor is advantageous because it provides all the components required for the core-shell structure and allows for the formation of highly crystalline and uniform core-shell NPs.

1.5 Nickel (II) Tetraphenylporphyrin (NiTPP)

Our previous work has focused on synthesizing and characterizing carbon-coated core-shell MNPs using iron-phthalocyanine and iron-porphyrin as precursors[30]. The study demonstrated the effectiveness of these precursors in producing

highly stable and MNPs suitable for biomedical applications. Building upon this foundation, we aim to explore the use of different metal centers within the porphyrin matrix to expand the potential applications and improve the properties of the resulting NPs. NiTPP is a promising precursor for core-shell synthesis in this context due to its unique chemical structure and properties.

NiTPP is an organometallic compound with the chemical formula $C_{44}H_{28}N_4Ni$ and with the nickel ion coordinated to a tetraphenylporphyrin ligand [31]. The tetraphenylporphyrin structure includes a macrocyclic ring composed of four pyrrole subunits connected via methine bridges (=CH-). Each pyrrole ring is bonded to a phenyl group, resulting in the tetraphenylporphyrin framework. The central nickel ion is coordinated within the nitrogen-containing cavity of the porphyrin ring, forming a stable complex, as shown in Figure 1.6. The boiling point of NiTPP is typically above 250°C, which makes it suitable for high-temperature synthesis processes such as solid-phase pyrolysis.

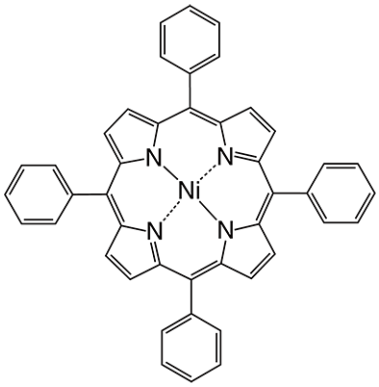


Figure 1.6: Molecular structure of Nickel(II) Tetraphenylporphyrin (NiTPP), a coordination compound where a nickel ion is centrally coordinated to a tetraphenylporphyrin ligand.

NiTPP is advantageous as a precursor for core-shell nanoparticle synthesis

for various reasons, such as providing the desired components necessary for forming core-shell MNPs with precise control over the core and shell composition [32], the presence of the nickel ion, and the extensive carbon framework of the porphyrin ligand facilitate the formation of a magnetic core with a protective carbon shell, the nickel ion contributes to the magnetic properties of the resulting NPs, and the ratio of carbon atoms to nickel atoms in NiTPP is also significant. With an extensive carbon framework surrounding the nickel center, the resulting core-shell MNPs benefit from enhanced stability and reduced oxidation, preserving their magnetic properties over time.

1.6 Magnetic Hyperthermia and Biomedical Applications

Cancer cells exhibit unique behaviors that distinguish them from normal cells, one of which is their ability to rapidly increase and form new blood vessels through a process known as angiogenesis[33]. This rapid growth necessitates an abundant supply of nutrients and oxygen, which the tumor achieves by stimulating the production of new blood vessels. Unlike the well-organized vasculature in normal tissues, tumor vasculature is typically disorganized and leaky. This characteristic allows for the enhanced permeability and retention (EPR) effect[34], where NPs and macromolecular drugs accumulate more readily in tumor tissues than in normal tissues.

Chemotherapy, currently the leading cancer treatment, has had a significant impact on patient survival rates and is widely used across various cancer types. However, its use is often accompanied by severe side effects due to its non-selective action, which harms healthy cells alongside cancerous ones[35]. These adverse effects can sig-

nificantly affect patients' quality of life and limit the overall efficacy of the treatment. Consequently, there is a growing need for more targeted and effective cancer therapies. Magnetic hyperthermia is a promising alternative that utilizes the properties of MNPs to selectively heat and necrotize the cancer cells, potentially reducing the collateral damage to healthy tissues.

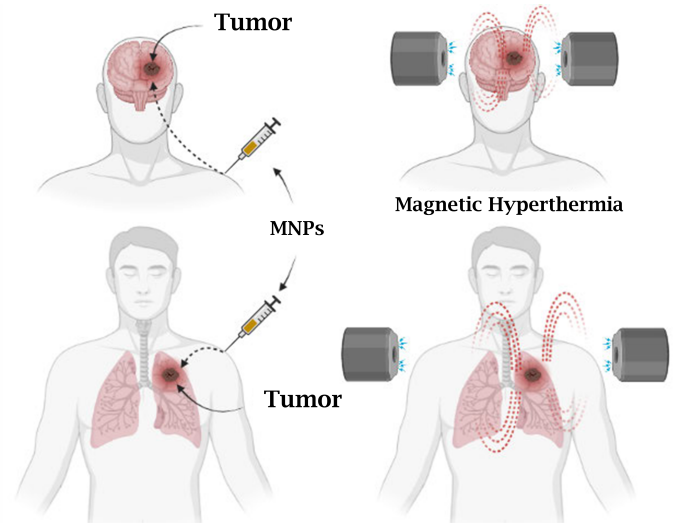


Figure 1.7: Schematic representation of magnetic hyperthermia treatment. MNPs are injected into the tumor site (left images). When subjected to an alternating magnetic field (right images), the MNPs generate localized heat, leading to the selective necrosis of cancer cells in tumors.

Magnetic hyperthermia involves using MNPs, which generate heat when subjected to an alternating magnetic field (AMF). The localized heating ranges between 43°C to 46°C[36] and can induce hyperthermia in the targeted tumor tissue, effectively destroying cancer cells while minimizing damage to surrounding healthy tissues. The heating efficiency of magnetic hyperthermia is influenced by various factors, including the amplitude and frequency of the applied alternating magnetic field, the magnetic anisotropy and magnetization of the particles, interactions between particles, and the size and size distribution of the MNPs[37,38,39].

This work is experimental and aims to achieve several objectives. Firstly, we sought to demonstrate the successful synthesis of core-shell MNPs using NiTPP as a precursor. Secondly, we intended to investigate the magnetic properties of these NPs, mainly focusing on optimizing the synthesis parameters. Lastly, we aim to explore the potential of NiTPP as a viable precursor for synthesizing MNPs suitable for biomedical applications, such as magnetic hyperthermia.

CHAPTER 2

Sample Synthesis and Experimental Technique

2.1 Sample and Ampoule Preparation

Preparing samples and ampoules is critical to successfully synthesizing carbon-coated NiTPP core-shell MNPs. The process begins with the selection and cleaning of quartz tubes. Quartz tubes are chosen for their ability to hold a vacuum and withstand temperatures up to 2200°C[40]. The tubes used in this research have an outer diameter of 12 mm and an inner diameter of 8 mm. Before any sample introduction, the quartz tubes are thoroughly cleaned to remove potential contaminants.

Once the quartz tubes are cleaned and dried, introducing the NiTPP precursor is the next step. NiTPP was purchased from PorphyChem Company with a minimum purity of 98%. The precursor is a purple solid in appearance, is stable at room temperature, and was used as-is. We accurately measure 100 mg of NiTPP using an analytical balance and carefully transfer it into the quartz tubes. Only plastic spatulas and weighing paper are used during this process to avoid contamination.

Achieving a high vacuum environment inside the quartz tubes is essential to prevent unwanted oxidation during pyrolysis. The open end of each quartz tube is connected to an Edwards Turbomolecular Pumping Station capable of reaching pressures as low as ten millitorr. The system consists of a mechanical pump followed by a turbo molecular pump to achieve the required low pressure. The tubes are kept

under vacuum for up to 15 minutes to ensure all air and moisture are removed.

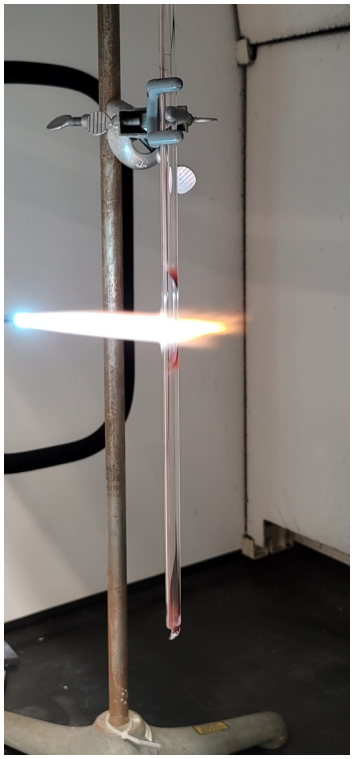


Figure 2.1: Sealing of a quartz ampoule using an oxy-acetylene torch. The ampoule contains precursor materials for the synthesis of carbon-coated core-shell nanoparticles.

Sealing the quartz ampoules under vacuum is performed using an oxy-acetylene torch, which can reach temperatures up to 3150°C[41], see Figure 2.1. The technique involves gradually heating the secured tube while rotating the flame around the tube's circumference to ensure uniform heat distribution. Initially, the torch's flame is kept further from the tube, producing less intensity to gently burn off any residual organic material stuck to the quartz tube walls. Then, the flame is brought closer and concentrated on the region to be sealed. Once the area to be sealed begins to glow white, total internal reflection is observed, indicating sufficient heating and the quartz becomes malleable. At this stage, gentle twisting and pulling motions are applied to

seal the tube, ensuring no leaks that could compromise the vacuum inside. Any tube showing signs of cracks or leakage is discarded and repeated with a new tube. The sealed quartz ampoules are then stored until they are ready for pyrolysis.

2.2 Solid-Phase Pyrolysis

Solid-phase pyrolysis (SPP) is used to synthesize the desired core-shell MNPs. This pyrolysis synthesis method closely follows the methods developed by our partners at the Institute for Physical Research, National Academy of Sciences of Armenia[12,32,42,43], and has been further improved by our recent work[30,44], involves heating the NiTPP precursor to high temperatures under vacuum conditions at varying temperatures. The vacuum prevents unwanted secondary reactions, ensuring the purity of the synthesized NPs. The goal is to thermally degrade the precursor, breaking the molecule's bonds down and transforming it into a soot-like material from which the NPs can be extracted. This method is preferred for its simplicity, green synthesis approach, and cost-effectiveness, allowing for the consistent production of NPs.

The prepared and sealed quartz ampoules are placed in a horizontal MTI OTF-1200X-II-UL two-zone tube furnace capable of precise temperature control, see Figure 2.2. The furnace can reach temperatures up to 1000°C; however, for this work, the temperatures were explicitly chosen to be 500°C, 700°C and 900°C. The pyrolysis reaction can be represented as follows:

$$\mathrm{Ni(C_{44}N_4H_{28})} \xrightarrow[-14\mathrm{H_2},-2\mathrm{N_2}]{T_{\mathrm{pyr}},t_{\mathrm{pyr}},P_{\mathrm{pyr}}} \mathrm{Ni} + 44\mathrm{C} \tag{2.1}$$



Figure 2.2: MTI OTF-1200X-II-UL two-zone tube furnace used for solid-phase pyrolysis. An attached gas tank supplies the necessary atmosphere to ensure controlled reaction conditions during annealing.

Where T_{pyr} is the pyrolysis temperature, t_{pyr} is the pyrolysis time, and P_{pyr} is the self-generated pressure in the vacuum ampoule. The heat ramp used for the pyrolysis process involves a gradual ramp-up to the desired temperature, followed by a sustained high-temperature phase and a controlled cooling period, see Figure 2.3.

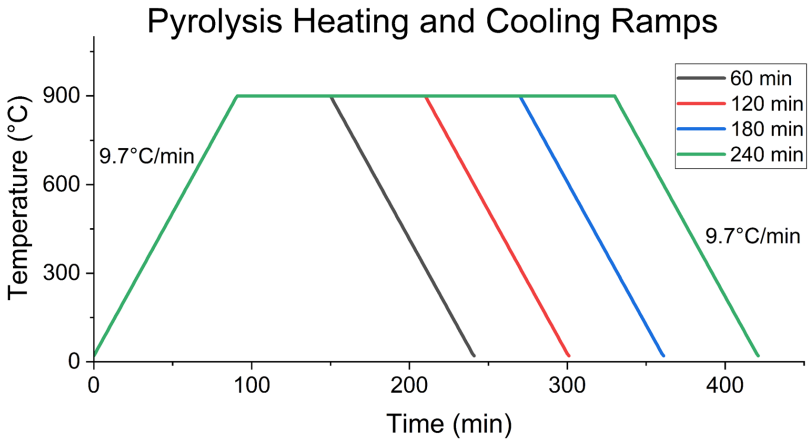


Figure 2.3: The diagram illustrates the temperature profiles for different durations of the pyrolysis process, including heating and cooling rates of 9.7°C/min. The color-coded lines represent different hold times at 900°C: 60 minutes (black), 120 minutes (red), 180 minutes (blue), and 240 minutes (green).

The specific heat ramps used in this research are as follows:

- **Ramp-Up Phase:** The temperature is increased from room temperature to the desired temperature (500°C, 700°C, and 900°C) at 9.7°C/min. This controlled ramp-up ensures that the thermal energy decomposes NiTPP gradually.
- **Sustained High-Temperature Phase:** Once the temperature reaches the desired temperature, it is held constant for 60, 120, 180, and 240 minutes. During this phase, the thermal energy is sufficient to decompose the NiTPP precursor completely. The high temperature facilitates the carbonization of the organic components and promotes the formation of carbon shells.
- **Cooling Phase:** After the sustained high-temperature phase, the furnace can cool down to room temperature at a controlled rate of 9.7°C per minute. This controlled cooling process allows the materials to solidify in a manner that promotes the proper assembly and stability of the core-shell nanoparticles.

Upon completion of the pyrolysis process, the ampoules are carefully removed from the furnace and stored until ready for deagglomeration. A common challenge of solid-phase pyrolysis is the formation of agglomerated and aggregated NPs. To address this, deagglomeration techniques are employed to separate the NPs from the remaining unwanted byproducts.

2.3 Annealing

The annealing process is a crucial secondary step in synthesizing core-shell NPs, aimed at modifying their structural and magnetic properties. Annealing, which

dates back to ancient China over 5000 years ago[45], involves heating the NPs to a specific temperature and maintaining them for a set period before cooling them gradually. This thermal treatment facilitates atomic and molecular reconfigurations, relieving internal stresses, enhancing crystallinity, and potentially inducing phase transformations[46]. By annealing the NPs in different environments, such as oxygen and nitrogen, we aim to investigate the effects of these atmospheres on the core-shell structure and overall properties of the NPs. This section details the annealing procedures used in this research, focusing on the methods and outcomes of annealing in both oxygen and nitrogen atmospheres.

Annealing is a widely utilized process in materials science and engineering to enhance various materials' physical and chemical properties[46,47]. The process consists of three phases, similar to pyrolysis: gradual heating, sustained heat, and gradual cooling (see Figure 2.4).

During the heating phase, the material is gradually brought to 150°C at a 3°C/min rate, known as the annealing temperature. The gradual increase in temperature avoids thermal shock and ensures uniform temperature distribution throughout the material. Typically, the annealing temperature is set below the material's melting point but high enough to facilitate atomic mobility.

The material is maintained at the annealing temperature for 180 minutes. This sustained heating period allows atoms to diffuse and reconfigure, leading to the relaxation of internal stresses, elimination of defects, and enhancement of crystallinity. Previous work in our lab determined the duration and temperature of the annealing process [30,44], which demonstrated the optimal annealing temperature and time.

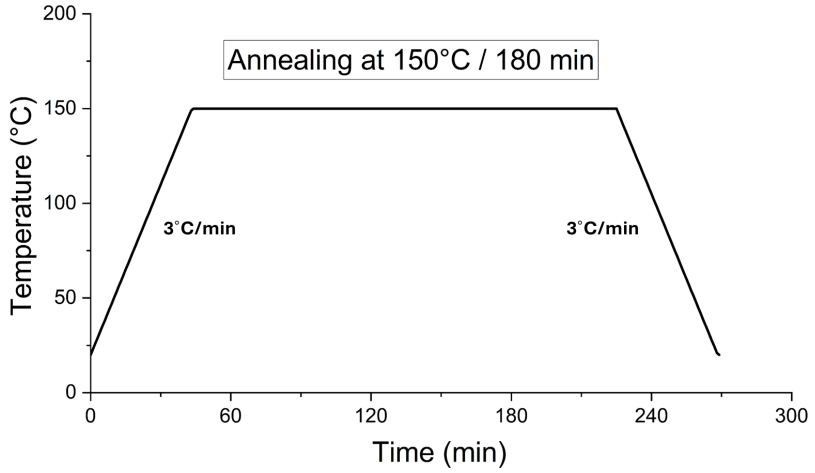


Figure 2.4: Annealing ramp used in the experiment.

The material is then gradually returned to room temperature at a 3°C/min rate. This cooling rate is critical, as it influences the material's final properties. Slow cooling generally promotes the formation of more prominent grains and a more stable crystalline structure, while rapid cooling, or quenching, can trap defects and produce a more amorphous structure.

Annealing can also induce phase transformations that enhance the material's properties when performed in a specific gas. For MNPs, annealing can significantly enhance coercivity, remanence, and saturation magnetization properties. Thus, the environment in which annealing is conducted plays a crucial role in determining the final properties of the material. An oxygen-rich atmosphere can lead to the formation of metal oxides while annealing in nitrogen-rich atmospheres promotes nitriding, which introduces nitrogen to the surface of a material. Therefore, by annealing NPs in different environments, we can tailor their structural and magnetic properties for specific applications.

2.4 Deagglomeration Process

As previously mentioned, the solid-phase pyrolysis method used in synthesizing core-shell NPs often results in forming agglomerated and aggregated particles. This occurs due to the high temperatures involved in the process, which can cause NPs to fuse together, leading to difficult to separate clusters. Deagglomeration is the process of separating these bound clumps of crystal aggregates into individual particles and dispersing them throughout a sample without further deterioration of the actual particles themselves.

After completing the pyrolysis process, the quartz ampoules containing the synthesized NPs are carefully cracked open using non-metallic tools such as plastic spatulas to avoid contamination. The samples are then collected into an agate mortar and pestle. To ensure thorough deagglomeration, both dry and wet grinding methods are employed. The samples are ground for approximately 45 minutes, alternating between dry and wet grinding to break down large aggregates and achieve a finer particle size.



Figure 2.5: Figure illustrates the steps and instruments implemented during the deagglomeration process.

Following the initial mechanical grinding, the samples are transferred into

microcentrifuge tubes for further processing. The next step involves ultrasonic dispersion, which uses high-frequency sound waves to break apart particle agglomerates and distribute them evenly throughout the sample. The microcentrifuge tubes containing the ground samples are placed in an ultrasonic dispersion wash machine. The samples undergo ultrasonication for 30 minutes, utilizing sound frequencies greater than 20 kHz. This process helps to disrupt the particle agglomerates and achieve a more uniform dispersion. The ultrasonic jewelry cleaning machine used in this process is equipped with multiple transducers to provide effective ultrasonic energy distribution. The temperature control of the ultrasonic bath is disconnected to prevent any temperature rise that could lead to unwanted chemical or physical changes in the NPs.

The samples are centrifugated to separate particles based on their mass after ultrasonic dispersion. The microcentrifuge tubes are placed in a centrifuge and spun for approximately 30 minutes. This process separates the NPs from the liquid medium, with heavier particles settling at the bottom of the tube and lighter particles remaining suspended.

The final step in the deagglomeration process involves magnetic separation to isolate the MNPs from any non-magnetic impurities or non-reacted precursors. The samples are placed in a magnetic separation rack equipped with neodymium magnets. The strong magnetic field generated by the neodymium magnets attracts the MNPs, causing them to accumulate at the sides of the tubes. The tubes are left in the magnetic rack overnight to ensure complete separation. The remaining liquid and non-reacted precursor are carefully removed using a pipette, leaving the purified

MNPs behind. The separated samples are then allowed to dry under vacuum inside a desiccator to facilitate the evaporation of any remaining liquid.

2.5 Powder X-ray Diffractometry

Powder X-ray diffractometry (PXRD) is used to characterize the synthesized NPs' crystalline structure and phase composition. PXRD operates on X-ray scattering and diffraction principles, where X-rays are directed at a crystalline sample, and the resulting diffraction pattern is recorded. The mechanism behind this technique is fundamentally described by Bragg's Law, which relates the angle of incidence and the wavelength of the X-rays to the spacing between the atomic planes in the crystal lattice. Bragg's Law is mathematically expressed as

$$n\lambda = 2d\sin\theta \tag{2.2}$$

where n is the order of reflection, λ is the wavelength of the incident X-rays, d is the distance between adjacent atomic planes, and θ is the angle of incidence at which constructive interference occurs. This constructive interference produces distinct peaks in the diffraction pattern, corresponding to the specific interplanar spacings within the crystal.

The Bruker D2 Phaser uses a copper (Cu) X-ray source with a λ of 1.54 Å. The diffractometer was set up with a divergence slit of 0.6 mm, an anti-air scatter slit of 2 mm, and other appropriate settings to ensure precise data collection. The sample was prepared by placing a small amount of the powdered NPs on a 0.1-millimeter

silicon-based diffraction plate. The measurement was conducted over a 10-100 degree 2θ range to identify all present phases.

The analysis of the PXRD data was performed using Profex, an open-source software for PXRD and Rietveld refinement. The current version used was Profex 5.2.8, which includes an internal structural database for reference. Profex allows for precise analysis and refinement of the diffraction data, facilitating the accurate determination of phase composition and structural parameters. By utilizing PXRD, we can confirm the successful synthesis of NiTPP core-shell NPs and investigate the structures and phases present depending on the different pyrolysis/synthesis times.

2.6 Scanning Electron Microscopy

Scanning Electron Microscopy (SEM) is used to gain insight into the surface morphology and provides an elemental analysis. This research used a ThermoFisher Axia ChemiSEM to inspect the NiTPP NPs. To prepare the samples for SEM, a small amount of the synthesized NP powder was placed on top of carbon double-sided tape tabs fixed to 12 mm SEM pins. The pin mount, capable of holding up to seven pins at a time, could be repositioned and rotated to observe different samples.

SEM operates by focusing a beam of electrons onto a spot volume of the sample, transferring energy to that spot. The bombarding electrons, known as primary electrons, dislodge electrons from the sample surface, referred to as secondary electrons. These secondary electrons are collected by a positively biased detector and converted into a signal. By sweeping the electron beam across the sample surface, SEM produces amplified signals and converts them into high-resolution images of the

sample's topography.

In addition to surface imaging, the ThermoFisher Axia ChemiSEM is equipped with energy-dispersive X-ray spectroscopy (EDS) for elemental analysis. EDS works by emitting an electron beam onto the sample, which ejects an electron from the inner shell of an atom in the sample. As an outer shell electron drops to fill the vacancy, it emits characteristic X-rays, as shown in Figure 2.6. The energy of these X-rays is analyzed to determine the sample's elemental composition. Brighter spots in the EDS SEM images typically indicate areas where heavier elements are present, as these elements backscatter electrons more effectively.

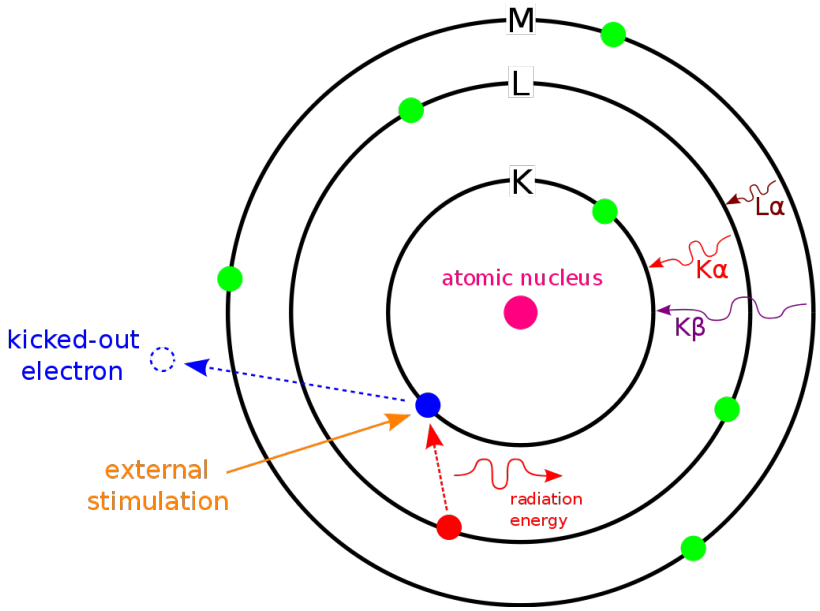


Figure 2.6: Schematic representation of Energy-Dispersive X-ray Spectroscopy (EDS). External stimulation causes an electron to be ejected from an atom's inner shell (K shell). As electrons from higher energy levels (L and M shells) fill the vacancy, characteristic X-rays, Kα, Kβ, and Lα are emitted, allowing for the identification of the sample's elemental composition.

For EDS analysis, the SEM beam was switched to the elemental analysis mode in the user interface. Random sites on each sample were chosen, and a count of at

least 10,000 readings was taken before moving to another site. This process was repeated until sufficient accuracy was achieved for the elemental analysis.

2.7 Vibrating Sample Magnetometry

Vibrating Sample Magnetometry (VSM) is used to measure the magnetic properties of materials. In this study, we employed the VSM attachment of the Quantum Design Physical Properties Measurement System (PPMS) to investigate the magnetic properties of NiTPP NPs. The PPMS is a system capable of performing a wide range of physical measurements, equipped with superconducting magnets and cryogenic temperature controls, capable of producing fields from ± 90 koersted or ± 9 Tesla and operating within a temperature range of 2-400 Kelvin[48].

The VSM operates on the principle of Faraday's law of electromagnetic induction. In the context of VSM, the sample provides the magnetic flux, and the induced voltage is detected in the pickup coils. The following equation describes this relationship:

$$V_{\text{coil}} = \frac{d\phi}{dt} = \frac{d\phi}{dz}\frac{dz}{dt} \tag{2.3}$$

Where ϕ is the magnetic flux, t is time, and z is the vertical position of the sample with respect to the coil. As the sample oscillates, the induced voltage follows a sinusoidal pattern, which the following equation can represent:

$$V_{\text{coil}} = 2\pi C m A \sin(2\pi f t) \tag{2.4}$$

Where C is a coupling constant, m is the magnetic moment of the sample, A is the

amplitude of oscillation, and f is the frequency of oscillation.

The sample preparation involves placing a minimum of 4 mg of the nanoparticle powder into a sample capsule, which is packed tightly and put onto a brass sample holder, allowing the tension force of the brass holder to secure the capsule in place. The brass sample holder is mounted onto a measuring station to align with the target line, as shown in Figure 2.7. Once the VSM is activated via the PPMS software, Multivu, the sample chamber is purged and prepared for measurement. The sample holder is screwed onto the sample rod and lowered into the chamber. The chamber is then closed, and the system auto-centers the sample.



Figure 2.7: PPMS sample holder secured in a brass sample holder and positioned in an alignment station.

Before taking any measurements, the sample needs to be demagnetized to ensure that the starting point of the measurement is near zero, roughly 10^{-7} to 10^{-5} emu. Demagnetization is performed by subjecting the sample to opposing magnetic fields so that the sample's magnetization stabilizes at zero emu in the absence of an applied field. Measurements are conducted by programming sequences to sweep the magnetic fields and temperatures as needed. Measurements include magnetization vs. magnetic field (M vs. H) hysteresis loops, which provide insights into the NPs' magnetic saturation, coercivity, and remanence. Magnetic measurements were taken at 10K and 300K temperatures and magnetic fields ranging from $\pm$10 koersted or $\pm$1

Tesla.

CHAPTER 3

Results and Discussion

This chapter presents the results obtained from the characterization of our synthesized NiTPP core-shell MNPs. The samples were systematically labeled based on their synthesis conditions and post-synthesis treatments to maintain a clear and consistent naming convention. This section includes SEM, PXRD, and VSM results, followed by a comprehensive discussion of the findings.

The samples were synthesized and classified based on their pyrolysis conditions and annealing environments. The precursor sample, labeled 'NiTPP Precursor,' was analyzed without undergoing pyrolysis or annealing, serving as a baseline to observe changes resulting from the pyrolysis process. Four different pyrolysis times (60, 120, 180, and 240 minutes) at 900°C were employed for the synthesized samples. Each synthesized sample was then divided into three parts: one part remained as-is, another was annealed in an oxygen atmosphere, and the third was annealed in a nitrogen atmosphere.

The naming convention used for the samples is as follows:

NiTPP900C60mC: Sample synthesized at 900°C for 60 minutes, as-is. NiTPP900C60mOC: Sample synthesized at 900°C for 60 minutes, annealed in oxygen. NiTPP900C60mNC: Sample synthesized at 900°C for 60 minutes, annealed in nitrogen. Similar naming is used for samples synthesized for 120, 180, and 240 minutes. The complete list of

samples is provided in Table 3.1 below:

Sample Name	**Description**
NiTPP Precursor	Pre Pyrolysis/Annealing
NiTPP900C60mC	Synthesized at 900°C for 60 minutes, as-is
NiTPP900C120mC	Synthesized at 900°C for 120 minutes, as-is
NiTPP900C180mC	Synthesized at 900°C for 180 minutes, as-is
NiTPP900C240mC	Synthesized at 900°C for 240 minutes, as-is
NiTPP900C60mOC	Synthesized at 900°C for 60 minutes, annealed in oxygen
NiTPP900C120mOC	Synthesized at 900°C for 120 minutes, annealed in oxygen
NiTPP900C180mOC	Synthesized at 900°C for 180 minutes, annealed in oxygen
NiTPP900C240mOC	Synthesized at 900°C for 240 minutes, annealed in oxygen
NiTPP900C60mNC	Synthesized at 900°C for 60 minutes, annealed in nitrogen
NiTPP900C120mNC	Synthesized at 900°C for 120 minutes, annealed in nitrogen
NiTPP900C180mNC	Synthesized at 900°C for 180 minutes, annealed in nitrogen
NiTPP900C240mNC	Synthesized at 900°C for 240 minutes, annealed in nitrogen

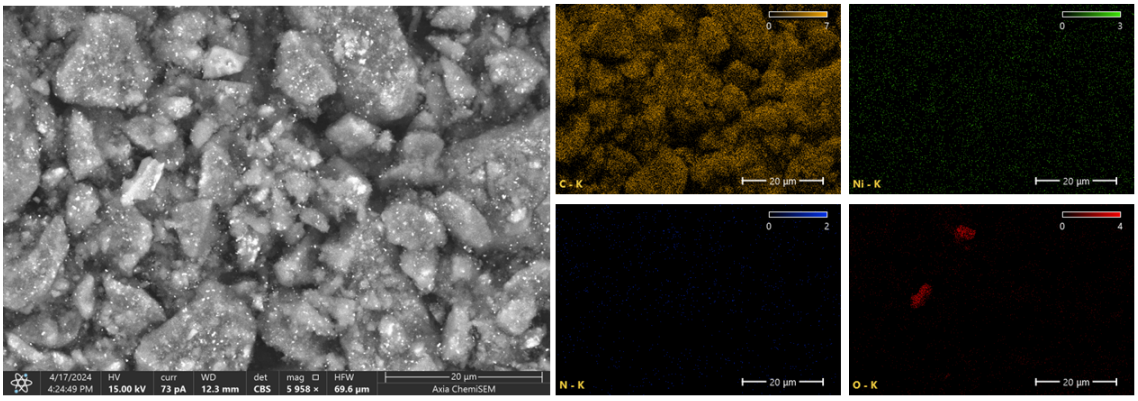
Table 3.1: Summary of NiTPP core-shell nanoparticle samples, their synthesis conditions, and treatments. All annealing was performed at 150°C for 180 min, with a gas flow rate of 100 sccm.

Our goal is to systematically evaluate how these synthesis parameters and annealing environments affect the emergence of magnetic core-shell structures and the overall properties of the NPs. This comparative approach helps us optimize the synthesis procedure for producing NiTPP MNPs by identifying the most effective

synthesis conditions and improving their magnetic characteristics for specific applications.

3.1 SEM Results

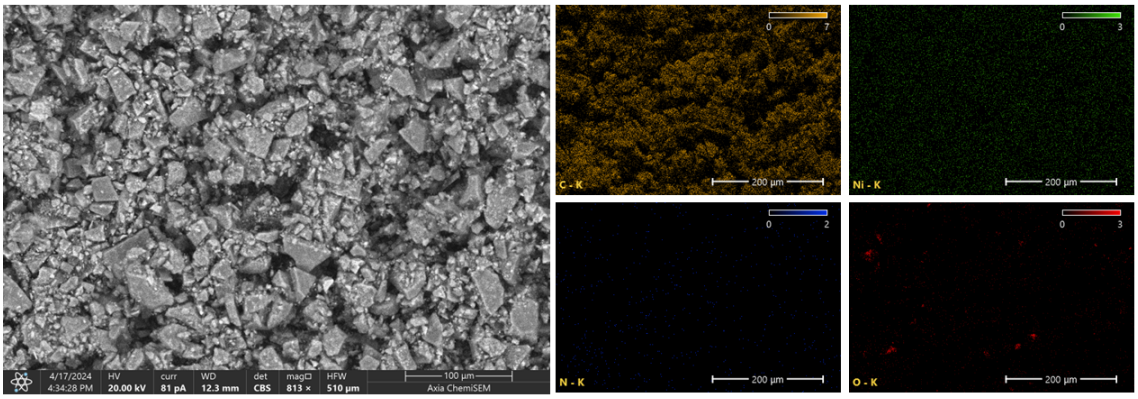
The SEM analysis of our samples provides a detailed examination of the morphology and elemental composition of the synthesized NiTPP-based MNPs. Each sample's structural characteristics and elemental distribution were scrutinized to understand the impact of synthesis and annealing conditions on the resultant NPs. It's important to note that the oxygen levels observed in the samples might be biased due to how we extract the synthesized sample from the quartz tube. Although we attempt to be as clean and efficient as possible by cleaning out residual quartz tube particles, some quartz tube particles inevitably remain when we crack them open, influencing the oxygen content.



Element	Atomic %	Atomic % Error	Weight %	Weight % Error	Net Counts
C	83.3	0.4	67.2	0.3	199445
Ni	5.4	0.1	21.4	0.4	11479
N	5.5	0.5	5.2	0.4	2940
O	5.8	0.2	6.2	0.3	5637

Figure 3.1: NiTPP900C60mC SEM image and EDS elemental mapping of the synthesized NiTPP nanoparticles, showing the distribution of nickel, carbon, nitrogen, and oxygen elements.

The SEM image of NiTPP900C60mC, Figure 3.1, reveals granular morphology with noticeable agglomeration of particles. The EDS elemental mapping shows a high concentration of carbon, accounting for 83.3% of the atomic composition, indicative of the carbon matrix. Nickel appears as bright spots scattered throughout the image, representing 5.4% of the atomic composition, suggesting the presence of nickel NPs embedded within the carbon matrix. Nitrogen and oxygen are present in smaller amounts, 5.5% and 5.8%, respectively, which are residues from the NiTPP precursor and possibly from quartz tube contamination.

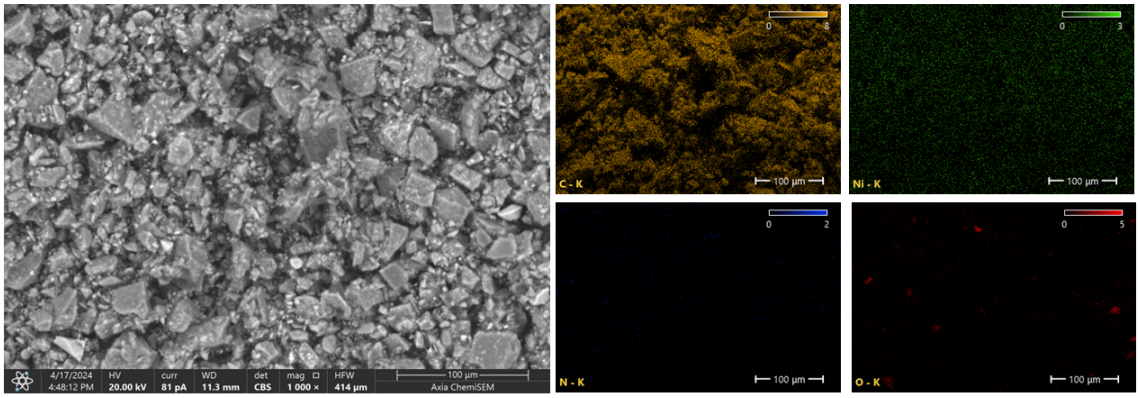


Element	Atomic %	Atomic % Error	Weight %	Weight % Error	Net Counts
C	83.0	0.4	66.2	0.3	121 003
Ni	5.8	0.1	22.6	0.3	25 561
N	5.4	0.6	5.0	0.5	1 809
O	5.8	0.3	6.2	0.3	3 577

Figure 3.2: NiTPP900C60mOC SEM image and EDS elemental mapping of the synthesized NiTPP nanoparticles, showing the distribution of nickel, carbon, nitrogen, and oxygen elements.

For NiTPP900C60mOC, which was annealed in oxygen, the SEM analysis displays a similar granular morphology to NiTPP900C60mC. The EDS mapping highlights a slightly increased nickel concentration at 5.8%, while carbon remains the dominant element at 83.0%. The presence of oxygen is 5.8%, which could be ei-

ther due to the annealing process or residual quartz left over, while nitrogen slightly dropped to 5.4%.

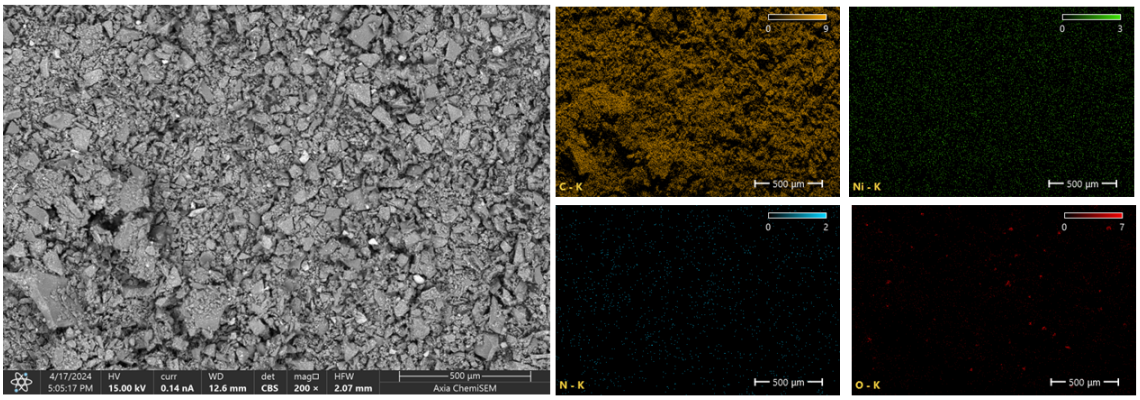


Element	Atomic %	Atomic % Error	Weight %	Weight % Error	Net Counts
C	82.8	0.4	67.1	0.3	204 342
Ni	5.2	0.1	20.8	0.2	38 682
N	5.5	0.5	5.2	0.4	2 978
O	6.4	0.2	6.9	0.3	6 357

Figure 3.3: NiTPP900C60mNC SEM image and EDS elemental mapping of the synthesized NiTPP nanoparticles, showing the distribution of nickel, carbon, nitrogen, and oxygen elements.

The sample NiTPP900C60mNC, annealed in nitrogen, exhibits a morphology consistent with the other 60-minute samples but with a distinct distribution of nickel NPs. The EDS mapping shows a nickel atomic percentage of 5.2%, slightly lower than the oxygen-annealed counterpart. Carbon remains high at 82.8%, while nitrogen and oxygen are at 5.5% and 6.4%, respectively, indicating minimal changes in composition due to the nitrogen annealing process. Quartz tube particles may also influence the observed oxygen levels.

The SEM image of NiTPP900C240mC, Figure 3.4, synthesized at 900°C for 240 minutes, reveals significant agglomeration. The EDS analysis shows a carbon concentration of 84.0% and a slightly higher nickel concentration at 6.1%, indicating



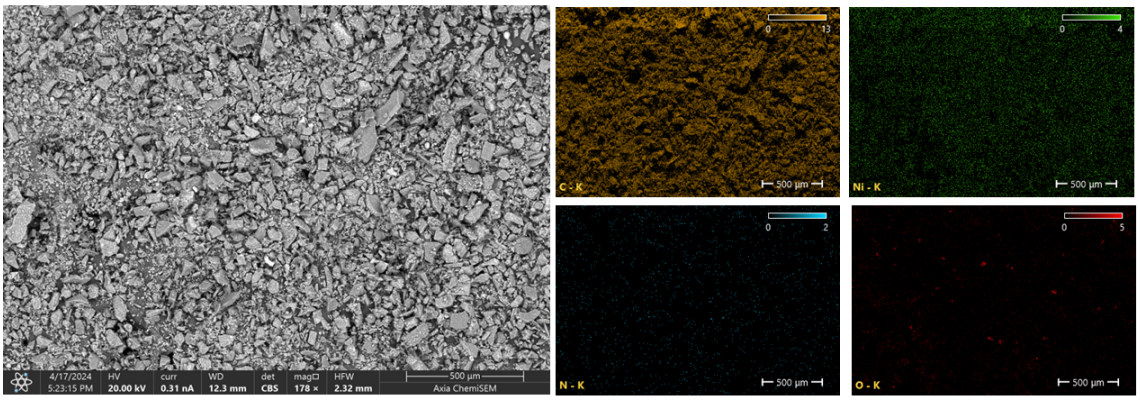
Element	Atomic %	Atomic % Error	Weight %	Weight % Error	Net Counts
C	84.0	0.4	66.4	0.3	303 994
Ni	6.1	0.1	23.8	0.4	20 873
N	5.1	0.3	4.7	0.3	4 297
O	4.8	0.2	5.1	0.2	7 573

Figure 3.4: NiTPP900C240mC SEM image and EDS elemental mapping of the synthesized NiTPP nanoparticles, showing the distribution of nickel, carbon, nitrogen, and oxygen elements.

a possible increase in nickel nanoparticle formation with extended synthesis time. Nitrogen and oxygen are at 5.1% and 4.8%, respectively, with residual quartz tube particles potentially affecting oxygen levels.

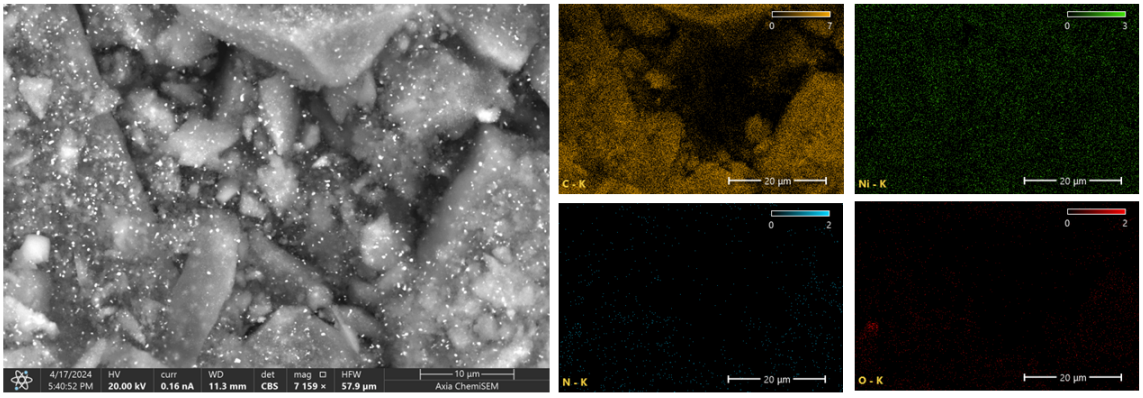
For NiTPP900C240mOC, Figure 3.5, the EDS mapping highlights a nickel atomic percentage of 5.0%, slightly lower than the non-annealed sample, possibly due to the oxidation process forming nickel oxide. Carbon is at 83.6%, and oxygen has increased to 6.2%, a potential increase due to the annealing procedure. Nitrogen is present at 5.1%.

Finally, the sample NiTPP900C240mNC, Figure 3.6, annealed in nitrogen, displays a granular morphology with a notable presence of nickel NPs as bright spots lodged throughout the carbon matrix. The EDS analysis shows a nickel concentration of 5.3%, consistent with the nitrogen annealing process. Carbon is 86.6%, while



Element	Atomic %	Atomic % Error	Weight %	Weight % Error	Net Counts
C	83.6	0.4	68.3	0.3	357 379
Ni	5.0	0.0	20.1	0.2	10 365
N	5.1	0.4	4.9	0.3	4 601
O	6.2	0.2	6.8	0.2	10 365

Figure 3.5: NiTPP900C240mOC SEM image and EDS elemental mapping of the synthesized NiTPP nanoparticles, showing the distribution of nickel, carbon, nitrogen, and oxygen elements.



Element	Atomic %	Atomic % Error	Weight %	Weight % Error	Net Counts
C	86.6	0.4	70.7	0.3	237 469
Ni	5.3	0.1	21.2	0.2	42 393
N	5.0	0.4	4.7	0.4	2 802
O	3.1	0.2	3.4	0.2	2 802

Figure 3.6: NiTPP900C240mNC SEM image and EDS elemental mapping of the synthesized NiTPP nanoparticles, showing the distribution of nickel, carbon, nitrogen, and oxygen elements.

nitrogen and oxygen are 5.0% and 3.1%, respectively.

The SEM analysis across all samples reveals a consistent granular morphology with varying degrees of agglomeration. The EDS elemental mapping confirms the

presence of nickel NPs distributed and embedded throughout the carbon matrix. There was no drastic increase in nitrogen content for samples annealed in nitrogen. In oxygen-annealed samples, although a slight increase in oxygen content was observed, it cannot be conclusively attributed to the annealing process due to the consistent presence of quartz. Additionally, SEM images are pending for the following samples: NiTPP900C120mC, NiTPP900C120mOC, NiTPP900C120mNC, NiTPP900C180mC, NiTPP900C180mOC, and NiTPP900C180mNC. This structural and compositional insight is crucial for understanding the synthesized NiTPP-based core-shell MNPs.

3.2 PXRD Results

The PXRD pattern of the NiTPP precursor provides a baseline for understanding the structural transformations occurring during pyrolysis. The PXRD results of the NiTPP precursor, shown in Figure 3.7, reveal distinct peaks corresponding to the crystalline nature of the organic compound. These peaks are consistent with previously reported data, particularly in the study by Brendan J. Kennedy et al. (1996) [49], which documented the crystallographic properties of NiTPP and similar compounds.

The precursor's diffraction pattern exhibits sharp peaks indicative of a well-defined crystalline structure. Key reflections observed include those around 10°, 20°, and 30° 2, corresponding to specific interplanar spacings in the NiTPP compound. These reflections will serve as reference points for identifying the phase transformations and the formation of the FCC structure of nickel NPs during and after the pyrolysis process. The transformation from the organic NiTPP to the FCC structure

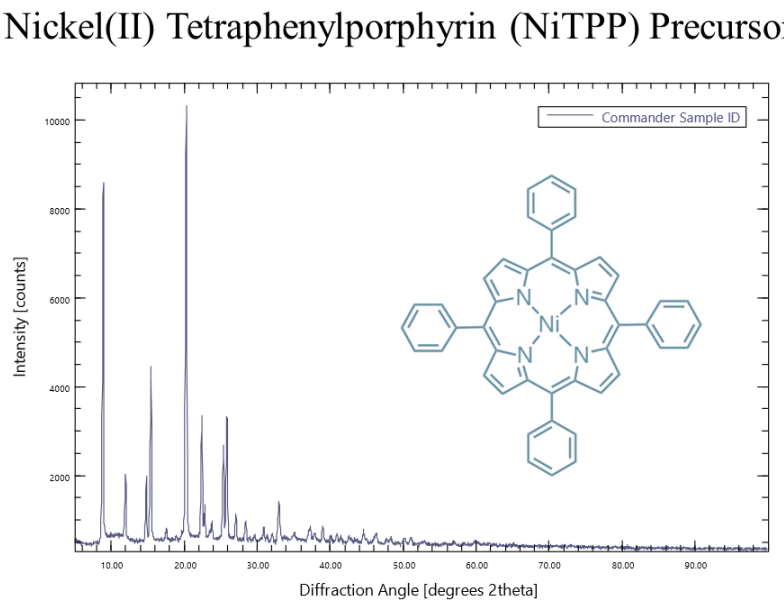


Figure 3.7: PXRD pattern of the Nickel(II) Tetraphenylporphyrin (NiTPP) precursor before pyrolysis. The peaks correspond to the crystalline structure of the organic compound.

of nickel NPs is marked by the disappearance of the precursor peaks and the emergence of new peaks corresponding to metallic nickel (Ni). This evolution highlights the thermal decomposition of the NiTPP precursor and the subsequent formation of nickel-based core-shell NPs, a primary focus of this study. The following sections present the PXRD results for the samples synthesized at 900°C for 60, 120, 180, and 240 minutes, with additional annealing in oxygen and nitrogen atmospheres.

NiTPP900C60mC: The PXRD pattern for the NiTPP900C60mC sample, shown in Figure 3.8a, displays prominent peaks corresponding to the face-centered cubic (FCC) structure of nickel, with notable reflections at (111), (200), (220), (311), and (222) planes. Additionally, peaks associated with carbon structures, including graphite 2H and 3R phases, are observed at around 26 degrees (2).

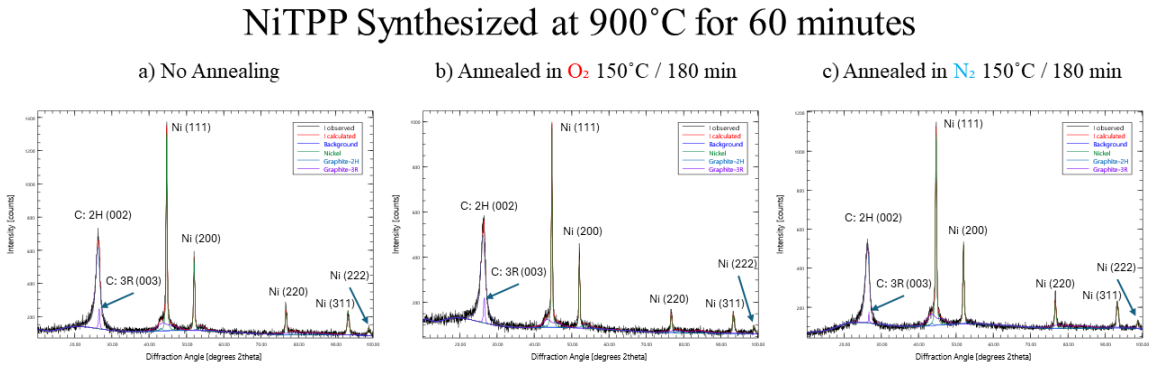


Figure 3.8: PXRD patterns of NiTPP synthesized at 900°C for 60 minutes: (a) No Annealing, (b) Annealed in O at 150°C for 180 minutes, and (c) Annealed in N at 150°C for 180 minutes.The diffraction peaks correspond to FCC Ni (111), (200), (220), (311), (222), and graphite (2H and 3R) structures.

NiTPP900C60mOC: Figure 3.8b shows the PXRD pattern for the NiTPP900C60mOC sample. The FCC nickel peaks are still prominent, but there is a slight shift and a slight broadening of peaks, possibly indicating the formation of nickel oxide phases due to the oxygen annealing. The carbon peaks remain consistent with the as-synthesized sample.

NiTPP900C60mNC: For the NiTPP900C60mNC sample, shown in Figure 3.8c, the PXRD pattern retains the FCC nickel peaks. The nitrogen annealing does not significantly alter the peak positions or intensities, suggesting that nitrogen annealing primarily affects the surface chemistry rather than the bulk crystalline structure.

NiTPP900C120mC: The PXRD pattern for the NiTPP900C120mC sample, as shown in Figure 3.9a, exhibits similar characteristics to the 60-minute sample, with clear FCC nickel peaks and carbon-related reflections. The increased synthesis time does not significantly alter the crystalline phases detected.

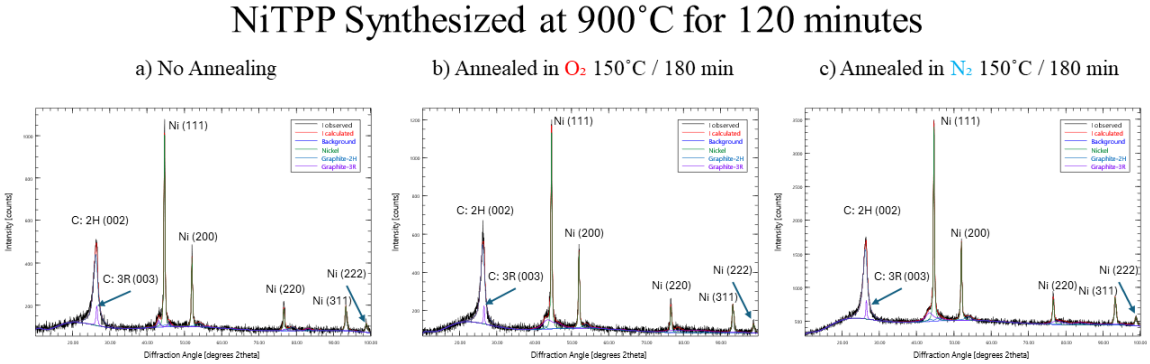


Figure 3.9: PXRD patterns of NiTPP synthesized at 900°C for 120 minutes: (a) No Annealing, (b) Annealed in O at 150°C for 180 minutes, and (c) Annealed in N at 150°C for 180 minutes.The diffraction peaks correspond to FCC Ni (111), (200), (220), (311), (222), and graphite (2H and 3R) structures

NiTPP900C120mOC: In Figure 3.9b, the PXRD pattern for the NiTPP900C120mOC sample shows FCC nickel peaks with very slight broadening, indicating some degree of oxidation. The carbon peaks remain sharp, consistent with previous observations.

NiTPP900C120mNC: Figure 3.9c presents the PXRD pattern for the NiTPP900C120mNC sample. The nitrogen annealing does not change the nickel peaks significantly, maintaining the FCC structure. The carbon peaks remain essentially unchanged.

NiTPP900C180mC: The PXRD pattern for the NiTPP900C180mC sample (Figure 3.10a) continues to show dominant FCC nickel peaks and carbon reflections. Prolonged synthesis time enhances the crystallinity of the nickel phase.

NiTPP900C180mOC: In Figure 3.10b, the PXRD pattern for the NiTPP900C180mOC sample shows a similar trend to previous oxygen-annealed samples, with slight broadening of nickel peaks and consistent carbon peaks.

NiTPP900C180mNC: The PXRD pattern for the NiTPP900C180mNC sample (Figure 3.10c) retains the FCC nickel peaks, with no significant changes due to

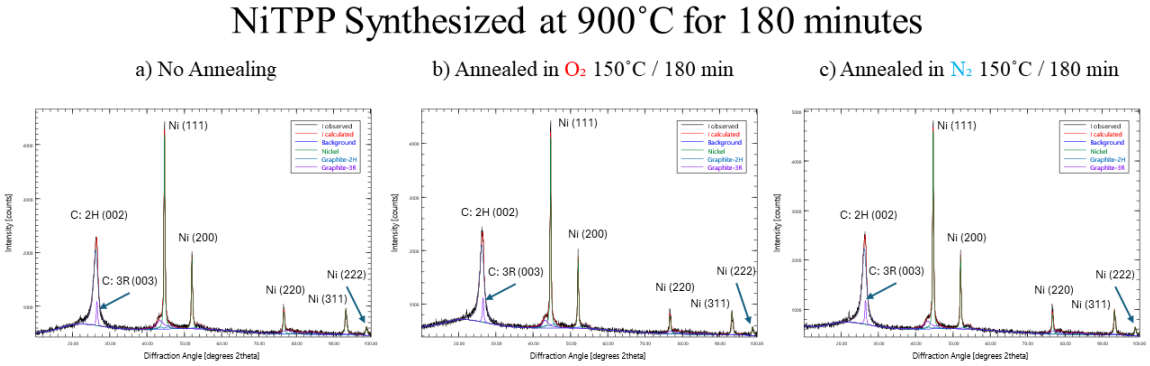


Figure 3.10: PXRD patterns of NiTPP synthesized at 900°C for 180 minutes: (a) No Annealing, (b) Annealed in O at 150°C for 180 minutes, and (c) Annealed in N at 150°C for 180 minutes.The diffraction peaks correspond to FCC Ni (111), (200), (220), (311), (222), and graphite (2H and 3R) structures

nitrogen annealing. The carbon peaks remain unchanged.

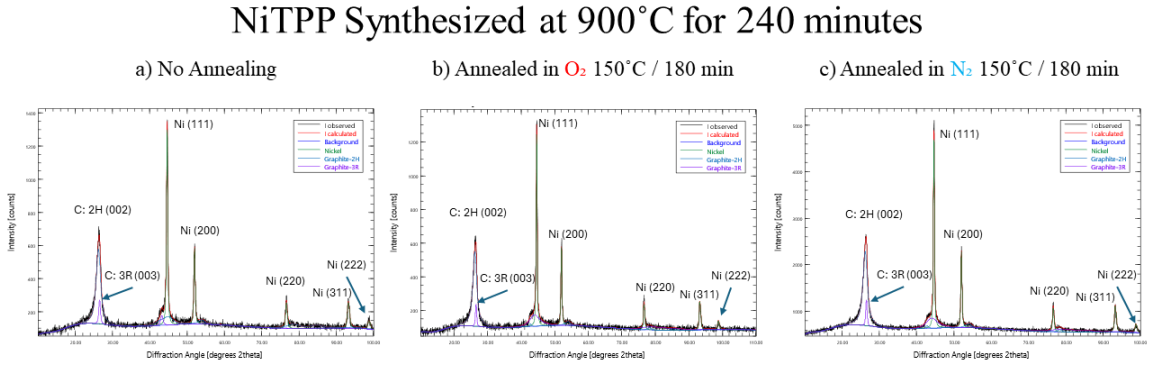


Figure 3.11: PXRD patterns of NiTPP synthesized at 900°C for 240 minutes: (a) No Annealing, (b) Annealed in O at 150°C for 180 minutes, and (c) Annealed in N at 150°C for 180 minutes.The diffraction peaks correspond to FCC Ni (111), (200), (220), (311), (222), and graphite (2H and 3R) structures

NiTPP900C240mC: The PXRD pattern for the NiTPP900C240mC sample, shown in Figure 3.11a, highlights the presence of well-defined FCC nickel peaks and sharp carbon peaks. The extended synthesis time enhances the peak intensities, indicating improved crystallinity.

NiTPP900C240mOC: Figure 3.11b displays the PXRD pattern for the NiTPP900C240mOC sample. Similar to previous oxygen-annealed samples, there is a very slight broadening of the nickel peaks, suggesting oxidation. The carbon peaks remain sharp and consistent.

NiTPP900C240mNC: For the NiTPP900C240mNC sample, shown in Figure 3.11c, the PXRD pattern retains the FCC nickel peaks, with no significant changes due to nitrogen annealing. The carbon peaks are consistent with those observed in the as-synthesized and oxygen-annealed samples.

The PXRD results consistently show the presence of the FCC structure of nickel across all synthesis and annealing conditions. The carbon matrix is indicated by the presence of graphite 2H and 3R phases. Oxygen annealing introduces slight broadening and shifting of nickel peaks, likely due to the formation of nickel oxide phases. Nitrogen annealing does not significantly alter the crystalline structure but may affect the surface chemistry of the NPs.

Using the Profex software, we calculated the grain sizes of the synthesized nickel NPs. Profex uses the Scherrer equation, which is applied to the peak broadening observed in the PXRD patterns to estimate the crystallite sizes. The grain sizes for the different samples synthesized at 900°C for varying durations and subjected to different annealing environments are presented in Table 3.2. The grain size calculations offer valuable insights into the impact of different synthesis and annealing conditions on the crystalline structure of the nickel NPs.

Sample Name	Calculated Grain Size (nm)
NiTPP900C60mC	37.4
NiTPP900C60mOC	31.8
NiTPP900C60mNC	42.4
NiTPP900C120mC	32.4
NiTPP900C120mOC	37.0
NiTPP900C120mNC	36.5
NiTPP900C180mC	32.4
NiTPP900C180mOC	32.5
NiTPP900C180mNC	33.9
NiTPP900C240mC	31.8
NiTPP900C240mOC	32.8
NiTPP900C240mNC	32.4

Table 3.2: Summary of the calculated grain sizes of nickel NPs synthesized at 900°C for various durations and annealed in O_2 and N_2 environments. Grain sizes were determined using Profex software through the application of the Scherrer equation to the PXRD data.

3.3 VSM Results

The Vibrating Sample Magnetometry (VSM) measurements provide detailed insights into the magnetic properties of our synthesized NiTPP samples under different conditions. The hysteresis loops were recorded at 10 K and 300 K for samples pyrolyzed at 900°C for varying durations and annealed in different atmospheres. The key parameters extracted from these measurements include saturation magnetization (M_s), remanent magnetization (M_r), coercive field (H_c), and the M_r/M_s ratio. Additionally, the estimated area under the hysteresis curves provides further insights into the magnetic behavior of the samples, specifically highlighting their heat generation capacity for applications such as magnetic hyperthermia.

The VSM results for the NiTPP precursor are presented in Figure 3.12. The

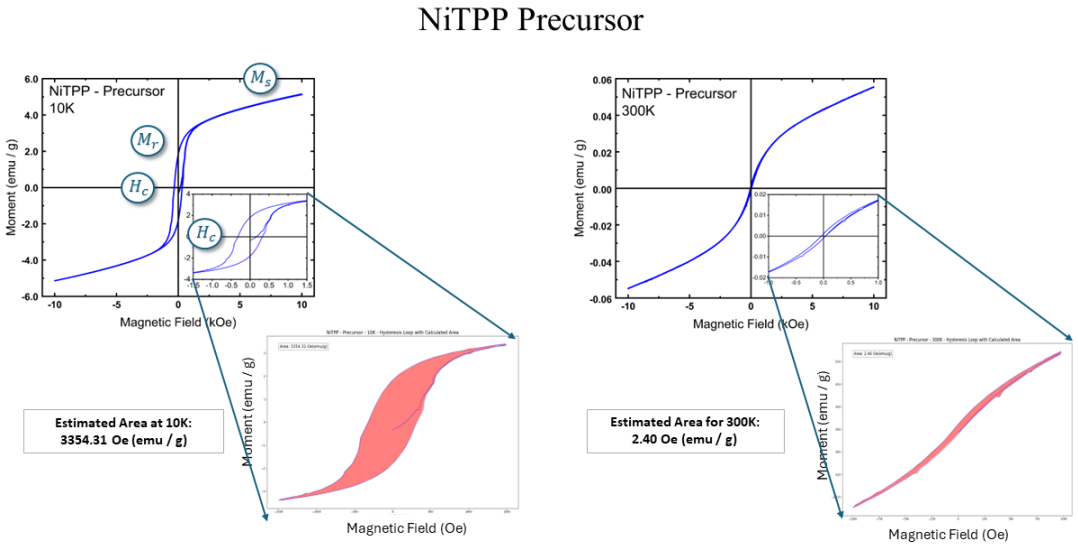
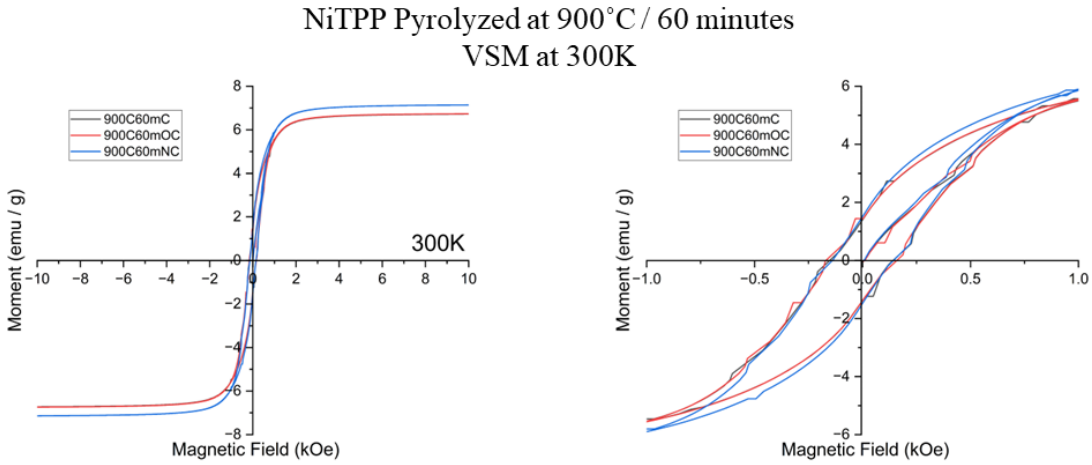


Figure 3.12: Hysteresis loops of NiTPP precursor measured at 10K and 300K.

hysteresis loops at 10K and 300K show very different magnetic behaviors compared to the pyrolyzed samples. At 10K, the precursor exhibits a small coercivity and remanent magnetization with an estimated area under the hysteresis curve of 3354.31 Oe (emu/g). In contrast, at 300K, the precursor displays paramagnetic behavior with a negligible hysteresis loop area of 2.40 Oe (emu/g). These observations indicate that the NiTPP precursor does not have significant magnetic properties before pyrolysis.

The VSM hysteresis loops for samples synthesized at 900°C for 60 minutes and measured at 300K are shown in Figure 3.13. The data reveal that the M_s values for the non-annealed (NiTPP900C60mC), oxygen-annealed (NiTPP900C60mOC), and nitrogen-annealed (NiTPP900C60mNC) samples are 6.72 emu/g, 6.73 emu/g, and 7.14 emu/g, respectively. The corresponding H_c values are 140.2 Oe, 169.4 Oe, and 141.5 Oe. The oxygen-annealed sample has the highest coercivity, showing a slightly increased M_r/M_s ratio compared to the non-annealed and nitrogen-annealed samples.

The hysteresis loops measured at 10K for the same set of samples are displayed



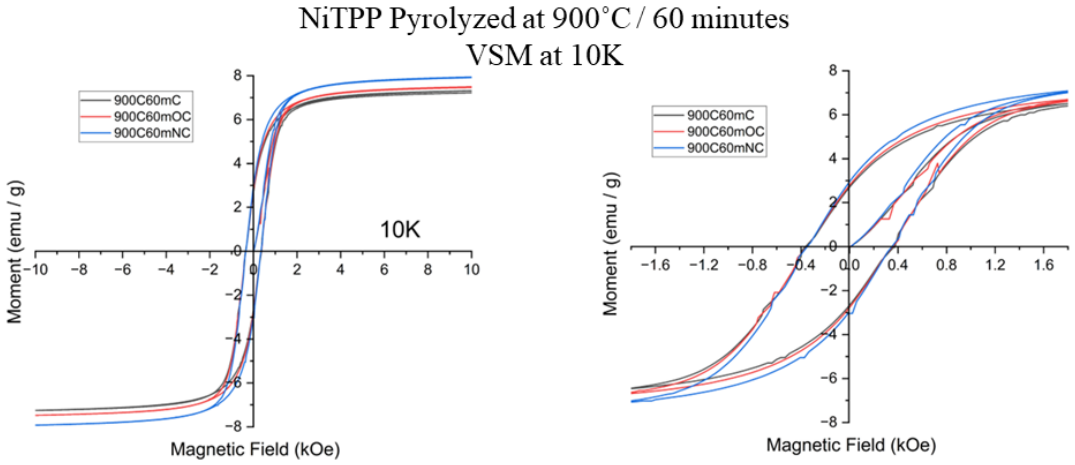
Sample	MvH Temp	Ms (emu/g)	Mr (emu/g)	Hc (Oe)	Mr/Ms	Estimated Area (Oe (emu/g))
NiTPP900C60mC	300K	6.72	1.42	140.2	0.211	2543.2
NiTPP900C60mOC	300K	6.73	1.44	169.4	0.214	2552.6
NiTPP900C60mNC	300K	7.14	1.51	141.5	0.212	2680.1

Figure 3.13: Hysteresis loops of NiTPP samples synthesized at 900°C for 60 minutes, measured at 300K.

in Figure 3.14. At this lower temperature, the M_s values are 7.31 emu/g, 7.49 emu/g, and 7.94 emu/g for NiTPP900C60mC, NiTPP900C60mOC, and NiTPP900C60mNC, respectively. The H_c values are significantly higher at 363.5 Oe, 348.9 Oe, and 347.5 Oe, reflecting the enhanced coercivity at low temperatures.

The hysteresis loops for the samples synthesized at 900°C for 120 minutes and measured at 300K are provided in Figure 3.15. The M_s values for NiTPP900C120mC, NiTPP900C120mOC, and NiTPP900C120mNC are 6.55 emu/g, 6.30 emu/g, and 6.57 emu/g, respectively. The H_c values are 130.8 Oe, 144.4 Oe, and 141.5 Oe, with the oxygen-annealed sample again showing the highest coercivity.

Figure 3.16 is for samples synthesized at 900°C for 180 minutes and measured at 300K. The M_s values are 6.54 emu/g, 6.84 emu/g, and 6.80 emu/g for



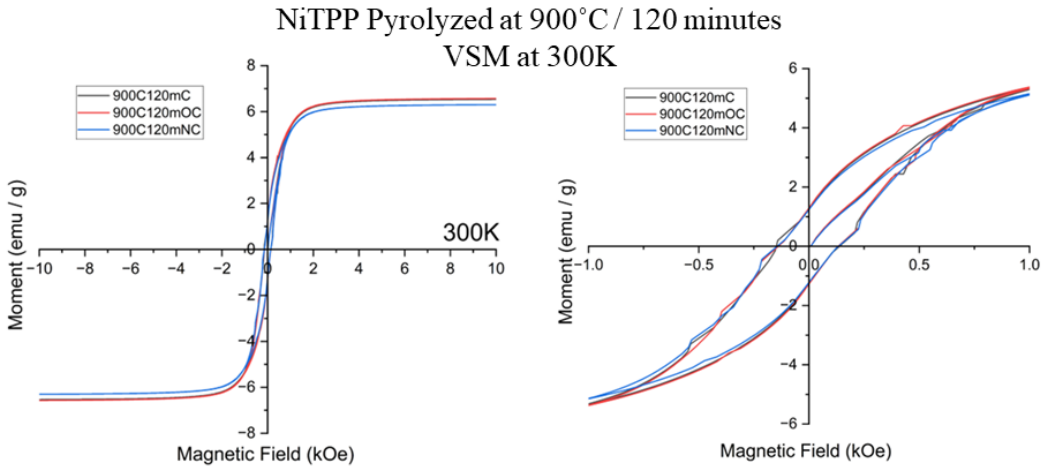
Sample	MvH Temp	Ms (emu/g)	Mr (emu/g)	Hc (Oe)	Mr/Ms	Estimated Area (Oe (emu/g))
NiTPP900C60mC	10K	7.31	2.70	363.5	0.369	7388.2
NiTPP900C60mOC	10K	7.49	2.76	348.9	0.368	7713.9
NiTPP900C60mNC	10K	7.94	2.95	347.5	0.372	8094.0

Figure 3.14: Hysteresis loops of NiTPP samples synthesized at 900°C for 60 minutes, measured at 10K.

NiTPP900C180mC, NiTPP900C180mOC, and NiTPP900C180mNC, respectively. The H_c values are 130.2 Oe, 138.8 Oe, and 136.8 Oe, indicating a consistent trend of increased coercivity in oxygen-annealed samples.

The hysteresis loops for samples synthesized at 900°C for 240 minutes and measured at 300K are depicted in Figure 3.17. The M_s values for NiTPP900C240mC, NiTPP900C240mOC, and NiTPP900C240mNC are 7.04 emu/g, 7.12 emu/g, and 7.21 emu/g, respectively. The H_c values are 150.4 Oe, 145.9 Oe, and 137.6 Oe, with a notable decrease in coercivity for the nitrogen-annealed sample.

The VSM results indicate that annealing in different atmospheres significantly affects the magnetic properties of the NiTPP NPs. The H_c) tends to increase with oxygen annealing across all time durations, suggesting the formation of nickel oxide

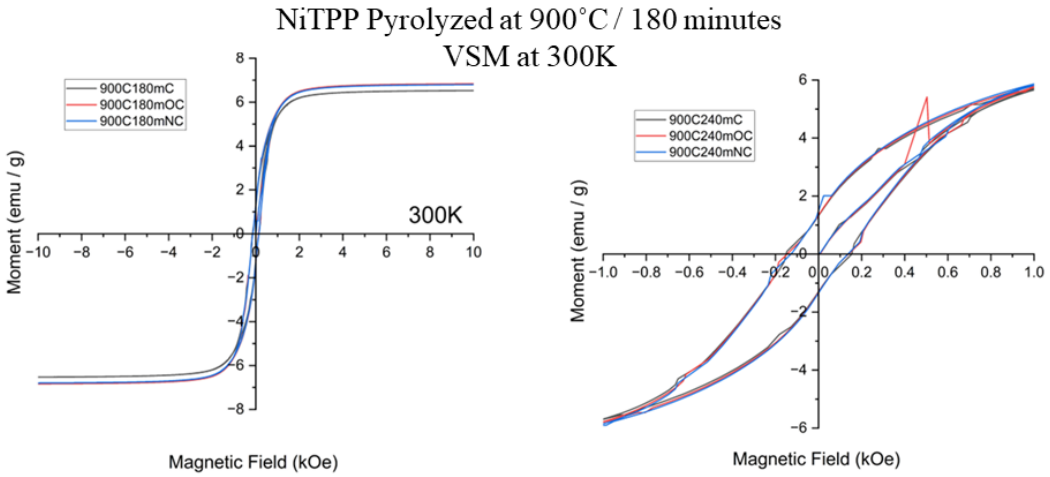


Sample	MvH Temp	Ms (emu/g)	Mr (emu/g)	Hc (Oe)	Mr/Ms	Estimated Area (Oe (emu/g))
NiTPP900C120mC	300K	6.55	1.28	130.8	0.195	2262.3
NiTPP900C120mOC	300K	6.30	1.26	144.4	0.200	2201.7
NiTPP900C120mNC	300K	6.57	1.29	141.5	0.197	2316.2

Figure 3.15: Hysteresis loops of NiTPP samples synthesized at 900°C for 120 minutes, measured at 300K.

or other magnetic phases that enhance coercivity. The nitrogen-annealed samples, while showing slight variations in H_c, do not exhibit a drastic change in nitrogen content, as confirmed by elemental analysis.

The increased M_s values at lower temperatures (10K) are consistent with typical ferromagnetic behavior, where thermal agitation is reduced, allowing for greater alignment of magnetic domains. The M_r/M_s ratios, which indicate the squareness of the hysteresis loop, are slightly higher in nitrogen-annealed samples, reflecting differences in magnetic domain interactions compared to oxygen-annealed and non-annealed samples.



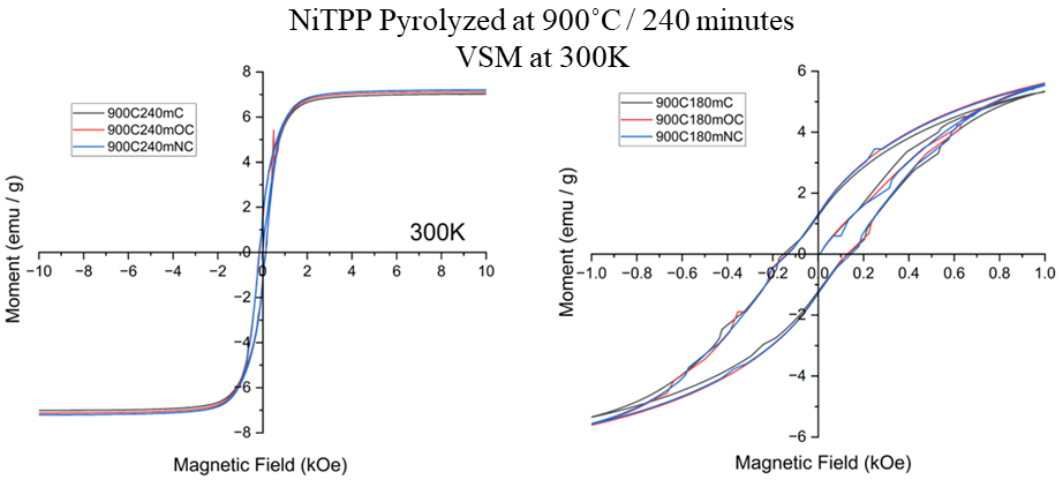
Sample	MvH Temp	Ms (emu/g)	Mr (emu/g)	Hc (Oe)	Mr/Ms	Estimated Area (Oe (emu/g))
NiTPP900C180mC	300K	6.54	1.27	130.2	0.193	2189.2
NiTPP900C180mOC	300K	6.84	1.35	138.8	0.198	2381.0
NiTPP900C180mNC	300K	6.80	1.31	136.8	0.193	2311.8

Figure 3.16: Hysteresis loops of NiTPP samples synthesized at 900°C for 180 minutes, measured at 300K.

3.4 Discussion

The comprehensive analysis of NiTPP precursor and pyrolyzed samples through PXRD, SEM, and VSM has provided significant insights into the structural and magnetic transformations induced by varying the solid-phase pyrolysis conditions. The precursor NiTPP, initially an organic compound, undergoes significant transformation upon pyrolysis, resulting in the formation of crystalline compounds featuring 2H and 3R carbon configurations and an FCC structure of nickel, indicative of nanoparticle formation.

PXRD analysis of the NiTPP precursor and synthesized samples revealed the emergence of distinct FCC nickel peaks and carbon phases post-pyrolysis. This transformation underscores the thermal decomposition of NiTPP into nickel NPs embedded



Sample	MvH Temp	Ms (emu/g)	Mr (emu/g)	Hc (Oe)	Mr/Ms	Estimated Area (Oe (emu/g))
NiTPP900C240mC	300K	7.04	1.34	150.4	0.190	2366.2
NiTPP900C240mOC	300K	7.12	1.37	145.9	0.192	2396.6
NiTPP900C240mNC	300K	7.21	1.39	137.6	0.193	3150.1

Figure 3.17: Hysteresis loops of NiTPP samples synthesized at 900°C for 240 minutes, measured at 300K.

within a carbon matrix. Notably, the PXRD patterns exhibited consistent FCC nickel peaks across various synthesis durations and annealing environments, signifying robust crystalline formation. Annealing in oxygen slightly broadened the nickel peaks, suggesting minor oxidation, whereas nitrogen annealing primarily affected surface chemistry without significantly altering the crystalline structure.

SEM and EDS analyses corroborated these findings by highlighting the samples' morphological changes and elemental distribution. The presence of nickel NPs was confirmed through EDS mapping, which showed nickel embedded throughout the carbon matrix. The carbon content remained high, while oxygen levels varied, potentially influenced by residual quartz tube particles. These observations suggest prolonged pyrolysis and annealing in specific environments can enhance nanoparticle

formation and crystallinity.

VSM measurements at 10K and 300K provided detailed insights into the magnetic properties of the synthesized samples. The NiTPP precursor displayed minimal magnetic properties, with negligible coercivity and remanent magnetization at 300K, indicative of paramagnetic behavior. In contrast, pyrolyzed samples exhibited significant magnetic characteristics, with M_s, M_r, and H_c varying based on synthesis and annealing conditions.

Annealing in oxygen consistently increased the H_c, suggesting the formation of magnetic phases like nickel oxide, which enhance coercivity. Nitrogen annealing, although not drastically altering the coercive field, showed slight variations indicating changes in surface chemistry. The M_s values were generally higher at 10K, consistent with typical ferromagnetic behavior, where reduced thermal agitation allows greater alignment of magnetic domains.

The estimated area under the hysteresis curves further highlighted the magnetic behavior and potential for heat generation in magnetic hyperthermia applications. Larger hysteresis loop areas correlate with greater heat dissipation, a critical factor for hyperthermia treatment. The results indicate that samples annealed in different environments show varying magnetic properties, potentially optimizing them for specific biomedical applications.

The synthesis and characterization of NiTPP-derived NPs provide a promising pathway for developing materials suitable for magnetic hyperthermia applications. The observed transformations and enhanced magnetic properties suggest that these NPs can generate significant heat under alternating magnetic fields, which is crucial

for targeted cancer treatment. The ability to tailor magnetic characteristics through controlled pyrolysis and annealing further enhances their applicability in biomedical fields.

Future work should focus on optimizing synthesis parameters and exploring the core-shell structure through high-resolution imaging techniques, such as HR-STEM. Additionally, comparing the magnetic and structural properties of NiTPP-derived NPs with those synthesized from other metalloporphyrins (e.g., CoTPP, CuTPP, ZnTPP) could provide broader insights into their potential applications and effectiveness in hyperthermia treatments.

In conclusion, the systematic study of NiTPP-derived MNPs underscores the importance of controlled synthesis and post-synthesis treatments in enhancing their structural and magnetic properties. These findings pave the way for developing advanced materials for biomedical applications, particularly in magnetic hyperthermia, offering a promising approach to targeted cancer therapy.

REFERENCES

[1] M. Faraday, *Experimental Relations of Gold (and Other Metals) to Light*, Philosophical Transactions of the Royal Society of London, 1857, 147, 145-181. https://doi.org/10.1098/rstl.1857.0011

[2] R. P. Feynman, *There's Plenty of Room at the Bottom*, Engineering and Science, 1960, 23(5), 22-36. https://calteches.library.caltech.edu/1976/1/1960Bottom.pdf

[3] G. Binnig and H. Rohrer, *Scanning Tunneling Microscopy – From Birth to Adolescence*, IBM Journal of Research and Development, 1987, 30(4), 355-369. https://doi.org/10.1103/RevModPhys.59.615

[4] H. W. Kroto, J. R. Heath, S. C. O'Brien, R. F. Curl, and R. E. Smalley, *C60: Buckminsterfullerene*, Nature, 1985, 318(6042), 162-163. https://doi.org/10.1038/318162a0

[5] S. Iijima, *Helical Microtubules of Graphitic Carbon*, Nature, 1991, 354(6348), 56-58. https://doi.org/10.1038/354056a0

[6] G. Oberdörster, E. Oberdörster, and J. Oberdörster, *Nanotoxicology: An Emerging Discipline Evolving from Studies of Ultrafine Particles*, Environmental Health Perspectives, 2005, 113(7), 823-839. https://doi.org/10.1289/ehp.7339

[7] K. T. Nguyen and Y. Zhao, *Integrated graphene/nanoparticle hybrids for biological and electronic applications*, Nanoscale, 2014, 6(12), 6245-6266. https://doi.org/10.1039/C4NR00612G

[8] X. Zhang, T. A. Le, and J. Yoon, *Development of a Real-Time Imaging-Based Guidance System of Magnetic Nanoparticles for Targeted Drug Delivery*, Journal of Magnetism and Magnetic Materials, 2017, 427, 345-351. https://doi.org/10.1016/j.jmmm.2016.10.056

[9] X. Liu, Y. Zhang, Y. Wang, W. Zhu, G. Li, X. Ma, and X. J. Liang, *Comprehensive understanding of magnetic hyperthermia for improving antitumor therapeutic efficacy*, Theranostics, 2020, 10(8), 3793. https://doi.org/10.7150/thno.40805

[10] H. Gleiter, *Nanostructured materials: basic concepts and microstructure*, Acta Materialia, 2000, 48(1), 1-29. https://doi.org/10.1016/S1359-6454(99)00285-2

[11] S. Laurent, D. Forge, M. Port, A. Roch, C. Robic, L. Vander Elst, and R. N. Muller, *Magnetic iron oxide nanoparticles: Synthesis, stabilization, vectorization, physicochemical characterizations, and biological applications*, Chemical Reviews, 2008, 108(6), 2064-2110. https://doi.org/10.1021/cr068445e

[12] A. Manukyan, A. Elsukova, A. Mirzakhanyan, H. Gyulasaryan, A. Kocharian, S. Sulyanov, M. Spasova, F. Römer, M. Farle, and E. Sharoyan, *Structure and size dependence of the magnetic properties of Ni@C nanocomposites*, Journal of Magnetism and Magnetic Materials, 2018, 467, 87-92. https://doi.org/10.1016/j.jmmm.2018.07.056

[13] S. Sun and H. Zeng, *Size-controlled synthesis of magnetite nanoparticles*, Journal of the American Chemical Society, 2002, 124(28), 8204-8205. https://doi.org/10.1021/ja026501x

[14] J. Livage, M. Henry, and C. Sanchez, *Sol-gel chemistry of transition metal oxides*, Progress in Solid State Chemistry, 1988, 18(4), 259-341. https://doi.org/10.1016/0079-6786(88)90005-2

[15] W. Y. Teoh, R. Amal, and L. Mädler, *Flame spray pyrolysis: An enabling technology for nanoparticles design and fabrication*, Nanoscale, 2010, 2(8), 1324-1347. https://doi.org/10.1039/C0NR00017E

[16] K. S. Suslick, *Sonochemistry*, Science, 1990, 247(4949), 1439-1445. https://doi.org/10.1126/science.247.4949.1439

[17] Y. M. Manawi, Ihsanullah, A. Samara, T. Al-Ansari, and M. A. Atieh, *A review of carbon nanomaterials' synthesis via the chemical vapor deposition (CVD) method*, Materials, 2018, 11(5), 822. https://doi.org/10.3390/ma11050822

[18] C. O. Kappe, *Controlled microwave heating in modern organic synthesis*, Angewandte Chemie International Edition, 2004, 43(46), 6250-6284. https://doi.org/10.1002/anie.200400655

[19] F. Fievet, S. Ammar-Merah, R. Brayner, F. Chau, M. Giraud, and F. Mammeri, *The polyol process: A unique method for easy access to metal nanoparticles with tailored sizes, shapes and compositions*, Chemical Society Reviews, 2018, 47(14), 5187-5233. https://doi.org/10.1039/C7CS00777A

[20] C. Suryanarayana, *Mechanical alloying and milling*, Progress in Materials Science, 2001, 46(1-2), 1-184. https://doi.org/10.1016/S0079-6425(99)00010-9

[21] E. Fazio, B. Gökce, A. De Giacomo, M. Meneghetti, G. Compagnini, M. Tommasini, F. Waag, A. Lucotti, C. G. Zanchi, P. M. Ossi, M. Dell'Aglio, L. D'Urso,

M. Condorelli, V. Scardaci, F. Biscaglia, L. Litti, M. Gobbo, G. Gallo, M. Santoro, and S. Trusso, *Nanoparticles engineering by pulsed laser ablation in liquids: Concepts and applications*, Nanomaterials, 2020, 10(11), 2317. https://doi.org/10.3390/nano10112317

[22] K. M. Krishnan, *Hysteresis*, In Fundamentals and Applications of Magnetic Materials (Reprint ed., pp. 76-95), Oxford University Press, 2020. ISBN: 978-0198862048.

[23] K. M. Krishnan, *An Overview of the Types of Magnetic Behavior in Materials*, In Fundamentals and Applications of Magnetic Materials (Reprint ed., pp. 50-75), Oxford University Press, 2020. ISBN: 978-0198862048.

[24] Wikipedia contributors, *Superparamagnetism*, In Wikipedia, The Free Encyclopedia, Retrieved May 25, 2024, from https://en.wikipedia.org/wiki/Superparamagnetism, 2023, May 20.

[25] T. Yanai, K. Eguchi, K. Koda, J. Kaji, H. Aramaki, K. Takashima, M. Nakano, and H. Fukunaga, *Investigation of coercivity for electroplated Fe-Ni thick films*, AIP Advances, 2018, 8(056123). https://doi.org/10.1063/1.5007293

[26] S. Manna, J. W. Kim, M. V. Lubarda, J. Wingert, R. Harder, F. Spada, V. Lomakin, O. Shpyrko, and E. E. Fullerton, *Characterization of strain and its effects on ferromagnetic nickel nanocubes*, AIP Advances, 2017, 7(125025). https://doi.org/10.1063/1.5004577

[27] M. Khatami, H. Q. Alijani, M. S. Nejad, and R. S. Varma, *Core@shell Nanoparticles: Greener Synthesis Using Natural Plant Products*, Applied Sciences, 2018,

8(3), 411. https://doi.org/10.3390/app8030411

[28] D. Tsamos, A. Krestou, M. Papagiannaki, and S. Maropoulos, *An Overview of the Production of Magnetic Core-Shell Nanoparticles and Their Biomedical Applications*, Metals, 2022, 12(4), 605. https://doi.org/10.3390/met12040605

[29] A. Adam and D. Mertz, *Iron Oxide@Mesoporous Silica Core-Shell Nanoparticles as Multimodal Platforms for Magnetic Resonance Imaging, Magnetic Hyperthermia, Near-Infrared Light Photothermia, and Drug Delivery*, Nanomaterials, 2023, 13(8), 1342. https://doi.org/10.3390/nano13081342

[30] F. Iglesias, C. Reynaga Gonzalez, J. Baughman, N. Wonderling, J. Shallenberger, A. Khodagulyan, O. O. Bernal, and A. N. Kocharian, *Characterization of carbon-coated core-shell iron nanoparticles annealed by oxygen and nitrogen*, AIP Advances, 2024, 14(025040). https://doi.org/10.1063/9.0000845

[31] A. L. Maclean, G. J. Foran, B. J. Kennedy, P. Turner, and T. W. Hambley, *Structural characterization of nickel (II) tetraphenylporphyrin*, Australian Journal of Chemistry, 1996, 49(12), 1273-1278. https://doi.org/10.1071/CH9961273

[32] A. T. Gyulasaryana, K. A. Castillo, O. O. Bernal, A. N. Kocharian, N. Sisakyan, G. K. Chilingaryan, A. A. Veligzhanin, J. L. Gray, E. G. Sharoyan, and A. S. Manukyan, *Synthesis and Structure of Fe-Fe3O4 Nanoparticles with "Core-Shell" Architecture Capsulated in a Graphite-Like Carbon Matrix*, Journal of Contemporary Physics (Armenian Academy of Sciences), 2021, 56(2), 150-153. http://doi.org/10.3103/S1068337221020079

[33] Q. Liu, Z. Guo, G. Li, and et al., *Cancer stem cells and their niche in cancer progression and therapy*, Cancer Cell International, 2023, 23, 305. https://doi.org/10.1186/s12935-023-03130-2

[34] Wikipedia contributors, *Enhanced permeability and retention effect*, In Wikipedia, The Free Encyclopedia, Retrieved April 22, 2024, from https://en.wikipedia.org/wiki/Enhancedpermeabilityandretentioneffect, 2023, April 10

[35] National Cancer Institute, *PDQ® Cancer Information Summaries*, In National Cancer Institute, Retrieved April 22, 2024, from https://www.cancer.gov/publications/pdq/information-summaries.

[36] I. M. Obaidat, B. Issa, and Y. Haik, *Magnetic properties of magnetic nanoparticles for efficient hyperthermia*, Nanomaterials, 2015, 5(1), 63-89. https://doi.org/10.3390/nano5010063

[37] S. Laurent, S. Dutz, U. O. Häfeli, and M. Mahmoudi, *Magnetic fluid hyperthermia: Focus on superparamagnetic iron oxide nanoparticles*, Advances in Colloid and Interface Science, 2011, 166(1-2), 8-23. https://doi.org/10.1016/j.cis.2011.04.003

[38] C. S. S. R. Kumar and F. Mohammad, *Magnetic nanomaterials for hyperthermia-based therapy and controlled drug delivery*, Advanced Drug Delivery Reviews, 2011, 63(9), 789-808. https://doi.org/10.1016/j.addr.2011.03.008

[39] R. Hergt, S. Dutz, R. Müller, and M. Zeisberger, *Magnetic particle hyperthermia: Nanoparticle magnetism and materials development for cancer*

therapy, Journal of Physics: Condensed Matter, 2006, 18(38), S2919-S2934. https://doi.org/10.1088/0953-8984/18/38/S26

[40] Wikipedia contributors. *Fused quartz*, In Wikipedia, The Free Encyclopedia, Retrieved April 2, 2024, from https://en.wikipedia.org/wiki/Fusedquartz.

[41] BOC Group. *Facts about acetylene*, Retrieved April 2, 2024, from https://www.boconline.co.uk/en/images/Facts-about-acetylenetcm410-262700.pdf.

[42] A. Manukyan, H. Gyulasaryan, A. Kocharian, P. Oyala, R. Chumakov, M. Avramenko, C. Sanchez, O. O. Bernal, L. Bugaev, and E. Sharoyan, *Structure and Magnetism of Few-Layer Nanographene Clusters in Carbon Microspheres*, The Journal of Physical Chemistry C, 2022, 126(1), 493-504. https://doi.org/10.1021/acs.jpcc.1c06748.

[43] A. S. Manukyan, A. A. Mirzakhanyan, T. K. Khachatryan, et al., *Copper-carbon nanocomposites prepared by solid-phase pyrolysis of copper phthalocyanine*, J. Contemp. Phys., 2012, 47, 292–295. https://doi.org/10.3103/S1068337212060084.

[44] Iglesias, F., *Synthesis and Magnetic Properties of Carbon-Coated Iron-Iron Oxide Core/Shell Nanoparticles*, Department of Physics and Astronomy, Master's Thesis, August 2022.

[45] Capable Machining. *Wärmebehandlung von Metallen im antiken China: Glühen, Abschrecken, Normalisieren und Anlassen.* Retrieved May 25, 2024, from https://capablemachining.com

[46] J. P. Mathew, G. Varghese, and J. Mathew, *Effect of post-thermal annealing on the structural and optical properties of ZnO thin films prepared from a polymer precursor*, Chinese Physics B, 2012, 21(7), 078104. https://doi.org/10.1088/1674-1056/21/7/078104

[47] J. P. Mathew, G. Varghese, and J. Mathew, *Effect of post-thermal annealing on the structural and optical properties of ZnO thin films prepared from a polymer precursor*, Chinese Physics B, 2012, 21(7), 078104. https://doi.org/10.1088/1674-1056/21/7/078104

[48] Quantum Design. *Physical Property Measurement System (PPMS)*, Retrieved March 13, 2024, from https://www.qdusa.com/products/ppms.html

[49] B. J. Kennedy, *Crystallographic properties of Nickel(II) Tetraphenylporphyrin*, Australian Journal of Chemistry, 1996, 49, 1273-1278. https://doi.org/10.1071/CH9961273